Cold Test 3, Run 2
Spartan IR Camera for the SOAR Telescope

Dustin I. Baker & Edwin D. Loh

Department of Physics & Astronomy
Michigan State University, East Lansing, MI 48824

`Loh@msu.edu`   517 355–9200 x2480

15 June 2007

Abstract

This note reports the results of Run 2 of Cold Test 3.

The Strehl at $\lambda 1523\,$nm is 0.86 for the high-res channel and 0.83 for the wide-field channel.

Detector #74 has a problem where segments of pixels have the same intensity, which makes this detector unusable. Teledyne replaced it with an engineering-grade detector and will send a science-grade detector when they make another batch.

A dark exposure is dominated by a light leak. The dark current increases with the ambient temperature, whereas a true dark current depends only on the detector temperature. The light leak at 21 C is 3–8 e^-/s, and the true dark current is in the range –0.3 to 1.5 e^-/s.

A full 7.5-L reservoir of liquid nitrogen lasts 21 hr, when the ambient temperature is 21 C. The heat load increased by $3 \pm 3\%$ over the 46-day run.

The pressure reading on the ion gauge rises 0.11 μTorr/day. If the residual gas is 60% He and 40% Ne, which is expected to be the case for permeation through the o-rings, then the actual pressure rise is 0.54 μTorr/day.

For an artificial star where the intensity of the central pixel is less than 17 kADU, the system is linear to 1%. The measurement is limited by drift in the light source.

The 4-eye detector mechanism did not move properly, which meant that the detectors were tilted with respect to the image plane. We suspect that two problems caused the strings that drive the mechanisms not to function properly. The teflon-coated quartz strings have an unexpectedly high thermal expansion. An aluminum block, inadvertently left in the instrument, may have been resting on one of the strings.

The DC level of the output of the electronics drifts unpredictably by a significant fraction of the range of the electronics. This causes the image to bottom out or saturate. This problem was fixed.

1 Introduction

For the results of Run 1 of Cold Test 3, see Baker & Loh 2006[1]

1.1 Tests

Focus Find the focus for one detector for the f/12 and the f/21 channels. Use the 1.523-μm laser, and the H-band filter to make the diffraction size determined by a single wavelength.

Focus across field Check whether the image size for the other 3 detectors matches that of the detector used for focusing.

Detector cosmetics Describe the cosmetic appearance of the four detectors. Are some quadrants usuable? Are there many hot spots?

Flexure Measure flexure for both the f/12 and f/21 channels. Use thermal radiation from the room. Take data in pairs separated by 5°. At the end, repeat the measurement at the starting orientation.

Dark current Use the dark slide. Measure with the instrument in the lab and outside in the cold to determine whether there is a light leak.

Detector noise Measure the noise *vs.* amount of light. Use the K-band filter. Use the stabilized incandescent light in a box. The box blocks solar radiation, which may vary because of clouds. Take pairs of pictures with the same exposure time. We found that the difference between the first pair is larger than subsequent pairs. Take at least 4 pairs.

Flat field Make a flat field by looking at paper illuminated by an incandescent light. Use a reduced pupil such as the "small pin-hole" pupil stop.

Offset of mechanism positioning between room temperature and 77 K. At the end of the cold test, use "Test Home" to find the reverse limit for all mechanisms. After the instrument is warm, use Test Home again. The difference is the offset of mechanism positioning between room temperature and 77 K.

---

[1]Baker, D., & Loh, E., 2006, Cold test 3, run 1, Spartan IR Camera for the SOAR telescope.

1.2   Installation

The bottom of the instrument is the side with the conflat vacuum opening for filter access. The window is on the front side.

The detector locations are named A1, A2, B1, and B2, where the "B" detectors are closer to the exterior of the instrument and the "2" detectors are toward the top (Figure 1).
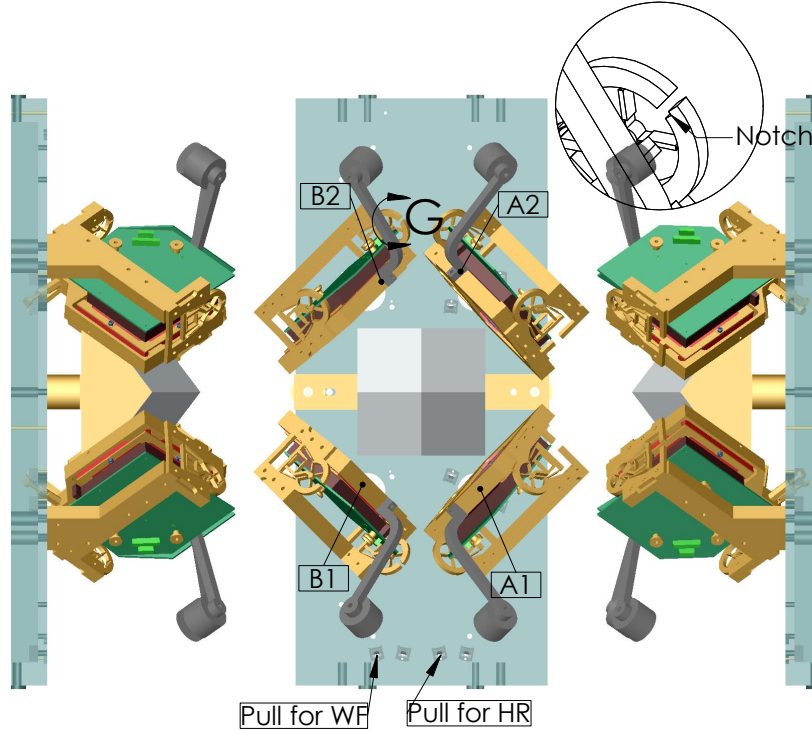

Figure 1: The 4-eye detector assembly shown in the wide-field configuration. Note the detector locations A1, A2, B1, and B2. The top of the instrument is at the top. The magnified detailed view shows the notch on the axles for the B detectors. The rotation axis, which points up before reflection by the pyramidal mirror, points NW, NE, NE, and NW for the A2, B2, A1, and B1 detectors, respectively, after reflection. The rotatation is right-handed for the wide-field configuration and left-handed for the high-res configuration.

The detectors are installed according to Table 2, and Table 1 shows their connections to the vacuum bulkheads and detector controllers. The channel numbers refer to the inputs on the umbilical board.

3

	Bottom					*Top*			
Pins	*Posn.*	*Contr.*	*Pins*	*Contr.*	*Pins*	*posn.*	*Contr.*	*Pins*	*Contr.*
20	A1	3			30	B2	7		
30	A1	3			20	B2	7		
20	nc		10	3	30	A2	2	10	nc
30	B1	5			20	A2	2		
20	B1	5			30	nc			
30	nc				20	nc			

Table 1: Vacuum bulkhead for the detector cables. The bulkhead is oriented as viewed from the air side; the 10-pin cable is to the right of the 20 and 30-pin cables.

Chan.	*Cont. SN*	*Loc.*	*Det. SN*	*Grade*
0	3	A1	24	Science
1	5	B1	92	Engineering
2	2	B2	74	Science
3	7	A2	66	Science

Table 2: Detectors. The channel number determines rotation of the FITS file. For Run 1 of Cold Test 3, channels 2 and 3 were swapped.
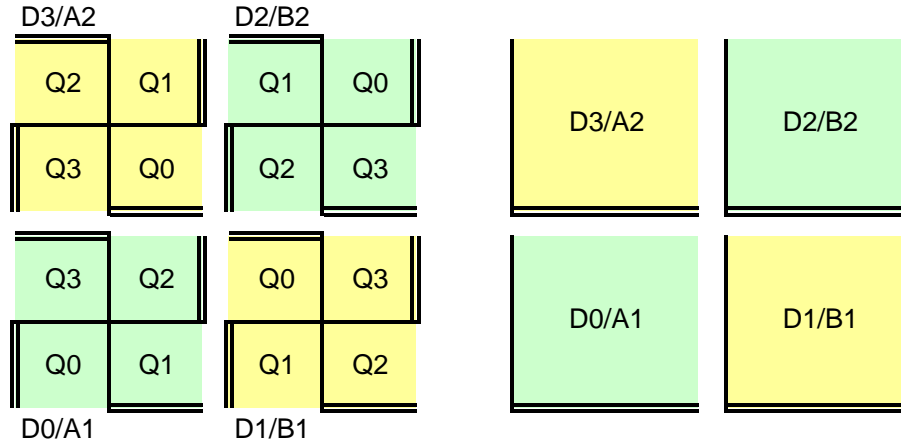

Figure 2: Detector arrangement. The x-axis, which changes more rapidly in the image file, is shown with double lines, and the single line is the y-axis. The right panels show the entire detector, and the left panels show the separate quadrants.

Pinholes on a mask plate are used to make artificial stars. See Figure 3 for their locations.
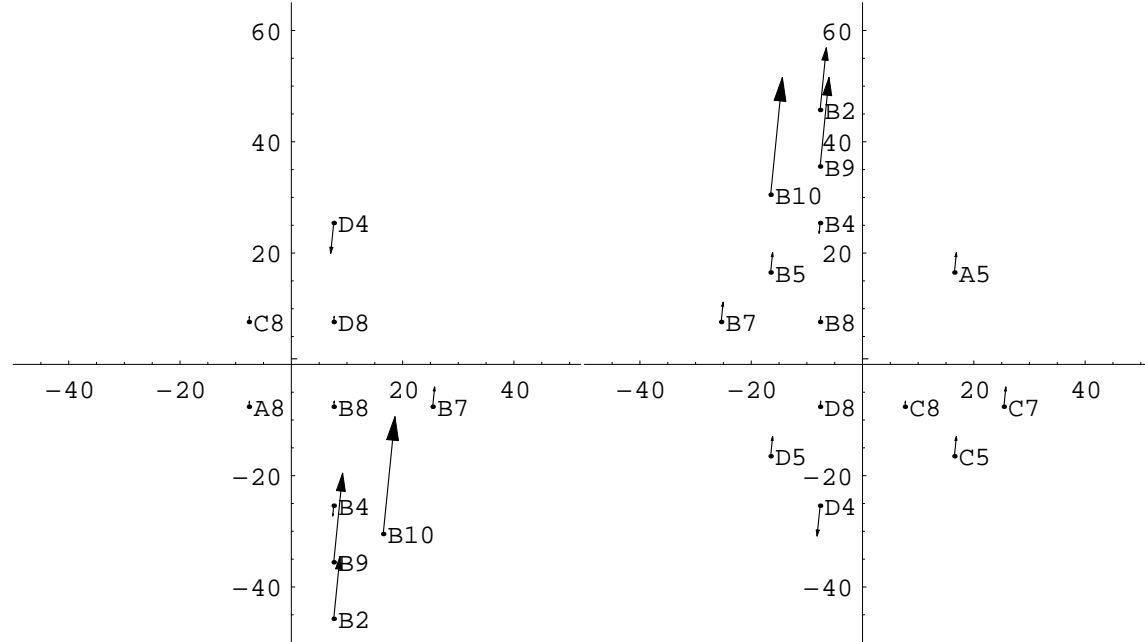
Figure 3: Pinholes for run 1 (left) and run 2 (right), as viewed from the front of the instrument with the top up. The arrows indicate depth of the pinhole magnified by 10, where up is toward the interior of the instrument. Pinhole C8 was not installed. If the mask is centered, the B, A, C, and D pinholes image onto the detectors in A1, B1, B2, and A2, respectively.

2   Shorted pixels on detector

#74

Science-grade detector #74 has a problem where segments of pixels have the same intensity, which makes this detector unusable. We call this problem "shorted pixels."[2]

Shorted pixels show in two ways. In the Figure 4, there are horizontal segments that are bright and segments that are dark. In addition, the correlation between columns is greater than that between row. The problem is hidden for the most part since the illumination is fairly uniform. It shows only where the intensity is abnormally high or low.

The problem is most easily seen in the vicinity of an artificial star (Table 3 and left of center in Figure 4). Here the illumination is nonuniform, and shorted
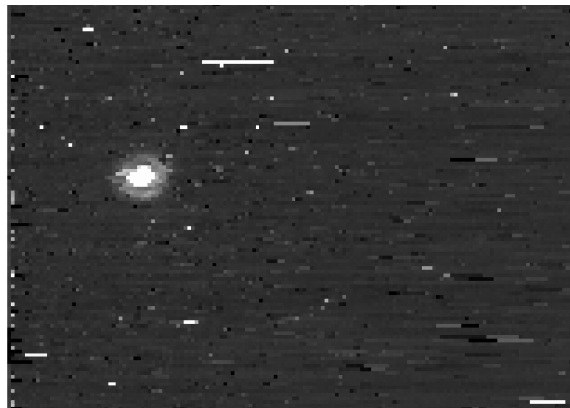

Figure 4: Artificial star imaged on a quadrant of detector #74 that is relatively free of shorted pixels. Note the shorted pixels, horizontal segments that have the same intensity.

pixels have the same intensity even though the intensity should be different because of the star.

Rockwell did not test for shorted pixels. The image of the dark current in the test report[3] of the detector shows this problem, but it is apparent only if one knows to look for it. Teledyne (Rockwell's successor) will now test for shorted pixels.[4]

Teledyne sent an engineering-grade detector to replace detector #74. When they make another batch of detectors, they will replace it with a science-grade detector.

3   Mechanisms

We installed a new antibacklash spring that does not use friction on the big filter wheel. We tested this for 2% of the expected lifetime of the instrument and found

---

[2]This section is taken from Loh, E., 2007, "Problem with HAWAII2 detector #74," which was sent to Teledyne.

[3]Rockwell Scientific, 2004, PACE HAWAII-2 FPA 74 Test Report.

[4]William Weissbard, 2007, private communication, Teledyne Corp.

164	162	166	168	232	217	232	232	291
160	208	234	236	222	214	210	200	176
182	264	268	246	248	504	742	734	482
242	<u>448</u>	<u>444</u>	<u>441</u>	<u>445</u>	1262	1804	1818	1784
440	426	369	<u>1514</u>	<u>1504</u>	<u>1502</u>	**3776**	2732	2716
204	210	<u>803</u>	<u>792</u>	<u>816</u>	<u>2632</u>	<u>2615</u>	<u>2597</u>	<u>2660</u>
242	244	388	960	1046	985	2524	2236	1306
154	306	346	360	760	758	753	756	364
284	281	281	276	276	245	252	238	240

Table 3: Intensity in the vicinity of the artificial star in Figure 4, which was taken with detector #74. Four clearly shorted regions are underlined. The center of the star is in bold face.

no problems (Baker & Loh 2007)[5]. We found no wear when we disassembled and inspected the spring.

We tested the mechanisms for the high-res collimator, the wide-field camera mirror, and 4-eye for 10% of the expected lifetime of the instrument (Baker & Loh 2007). One quartz string was frayed at a roller bearing, because the angle of the bearing was not set accurately enough. We have modified the installation instructions for the roller bearings.

The forward limit switch on the big filter wheel engaged when the rotation stage reached the forward limit but did not disengage when the rotation stage moved off of it. This is the same problem that we encountered with the reverse limit switch on the wide-field camera mechanism. The other forward limit switches work properly. This is the first time we tested the forward limit switches. The faulty switch has been replaced.

The mechanism for the mask wheel made a grinding noise for the first few moves and the mechanism lost positioning. The temperature of the mask wheel changed from 83 to 87 K when this occurred. See the temperature change at day 3.9 in Figure 14. Within 10 min, the mechanism ceased to make the grinding noise and worked perfectly. We plan to install a Prismatics motor driver, which can supply more current than the current NI motor driver. (The mask wheel is the only mechanism using the less powerful motor driver.)

The 4-eye mechanism is not seating (§10). There are two possible causes. First, the teflon-coated, quartz strings (McMaster 6373K89) that drive the mechanism

---

[5]Baker, D., & Loh, E., 2007, Lifetime tests of the mechanisms, Spartan IR Camera for the SOAR telescope

have an unexpectedly high thermal expansion. We had assumed that the thermal expansion is that of fused silica, which is very low compared to that of aluminum. To compensate for the contraction of the cryo-optical box, we installed a 200-mm length of teflon in the string path. However, we measured the thermal expansion of the string and found it to be 70% that of aluminum. The teflon section overcompensates and causes the string to be looser. This may be the reason that 4-eye does not seat properly.

The second possible cause for 4-eye not seating is a 25x12x100-mm block of a aluminum that was inadvertantly left in the instrument. It may have rested against the strings at some orientations of the instrument.

4   Image Quality

To measure the image quality, we feed the instrument a perfect artificial star. The artificial star is a pinhole on the mask illuminated by a 1523-nm laser. Because diffraction through the 5 or 8-μm pinhole is wide, the beam illuminates the pupil uniformly. The intensity at radius r from the center of the pupil is $I(r) = 4(J_1(u)/u)^2$, where $u = \pi r/(f\lambda)$, f is the focal ratio, and λ is the wavelength. The pupil is apodized slightly: The intensity at the edge of the f/16 beam is 0.974, 0.935, and 0.502 that at the center for pinhole of diamter 5, 8, and 25 μm, respectively. (The 25-μm pinholes were not used to measure image quality.)

The artificial star is unaberrated because the wavefronts from it are spherical.

The pinholes for creating artificial stars are put in wells on the mask plate. (See Figure 3 for a schematic and Figure 7 for an image taken by the instrument.) The depths of the wells match the curved field of the telescope. The mask is rotated to change the focus. A few of the wells are especially deep, and a few of the pinholes are put on washers to widen the range of focus.

Focusing is done by changing the axial position of the pinhole and maximizing s_r the "Strehl surrogate," which is defined to be the amount of light in the central pixel relative to the light within radius r. (The light is included for the pixels for which the center of the pixel is within r of the centroid of the image.)

The Strehl surrogate must be corrected for centering, since the light in the brightest pixel drops as the image is moved off center. Appendix A gives the correction for centering for an in-focus image. The correction for centering is large for the wide-field channel, since the image is undersampled.

If the image is out of focus, the image is not sharp, and the correction for centering is less. We did not compute corrections for out-of-focus images, but one can estimate the effect from Figure 8.41 of Born & Wolf, which is a plot of the intensity contours in

8

the directions parallel and perpendicular to the optic axis. The correction $ds_r(x) = s_r(x) - s_r(0) \approx \frac{dI(r)}{dr}x^2$. In the diffraction peak and outside of the geometric shadow, the contour lines are straight and parallel to the optic axis, which means $\frac{dI}{dr}$ is a constant. Therefore the correction to the Strehl surrogate is constant outside of the geometric shadow, and the computed correction is accurate if the axial position at the mask is within $2r_\mathrm{d}f_\mathrm{m}^2/f_\mathrm{d} = 0.45\,\mathrm{mm}$ of focus for the wide-field channel and $0.24\,\mathrm{mm}$ for the high-res channel. (r_d is the "radius" of the detector; f_m and f_d are the focal ratios at the mask and the detector.) Outside of the geometric shadow, the contour lines widen, and the size of the correction decreases.

The measurement of the Strehl surrogate (the intensity in the brightest pixel) as a function of the axial position of the pinhole is shown in Figure 5. For the high-res channel, two detectors were used. The Strehl surrogate fits the axial distribution of light $I_a(z)$ in the center of a diffracted image, $I_a(z) = (\sin u/u)^2$, where $u = z\pi/(8f^2\lambda)$.[6] We do not use the correction for $z_\mathrm{ph} = -1.5\,\mathrm{mm}$, since the correction should decrease outside of $0.24\,\mathrm{mm}$ of focus.

For the wide-field channel, the fit to $I_a(z)$ is poor, because the width of a pixel is a substantial fraction of the diffraction width. Instead we fit to $\frac{1}{2}I_a(z) + \frac{1}{2}I_r(r_d)$, a function derived from the form of the isophotal contours of Figure 8.41 of Born & Wolf. ($I_r(r_d)$ is the radial intensity.) This function is valid outside of the geometric shadow, but we none the less use it beyond that range. We do not use the correction for $z_\mathrm{ph} = -1.2\,\mathrm{mm}$, since the correction should decrease outside of $0.45\,\mathrm{mm}$ of focus.

To convert from the Strehl surrogate to Strehl, we compute the amount of light in the central pixel. The Lyot stop has a central blockage, which is meant to block the secondary mirror of the telescope. The radius of the central blockage is 0.32 of the radius of the pupil for the wide-field channel and 0.29 for high-res channel. The laser wavelength is 1523 nm.

The Strehl at $\lambda1523\,\mathrm{nm}$ (Table 4) is 0.86 for the high-res channel and 0.83 for the wide-field channel. This result depends on an accurate computation of the expected amount of light in the central pixel. The pixel size p affects the inferred Strehl by $d\log\mathrm{Strehl} = -d\log p$. An accuracy of 5% for the Strehl ratio requires knowing the plate scale to 5%.

The Strehl is 6–12% lower than expected. The measured RMS of the mirror surfaces are 5, 9, 11, 12, and 17 nm for the fold mirrors, wide-field collimator, wide-field focusing mirror, high-res collimator, and high-res focusing mirror, respectively.[7] The light from a given point in the field illuminates a subaperture, a part of a mirror, and the surface accuracy is that for the worst subaperture. The worst error is used,

---

[6]Born, M., & Wolf, E., 1970, *Principles of Optics*, 4th ed., Oxford: Pergamon, p. 441.

[7]Warren, M., 2003, Test report for the f/11 mirrors, Axsys Technology document 1992-950-00.
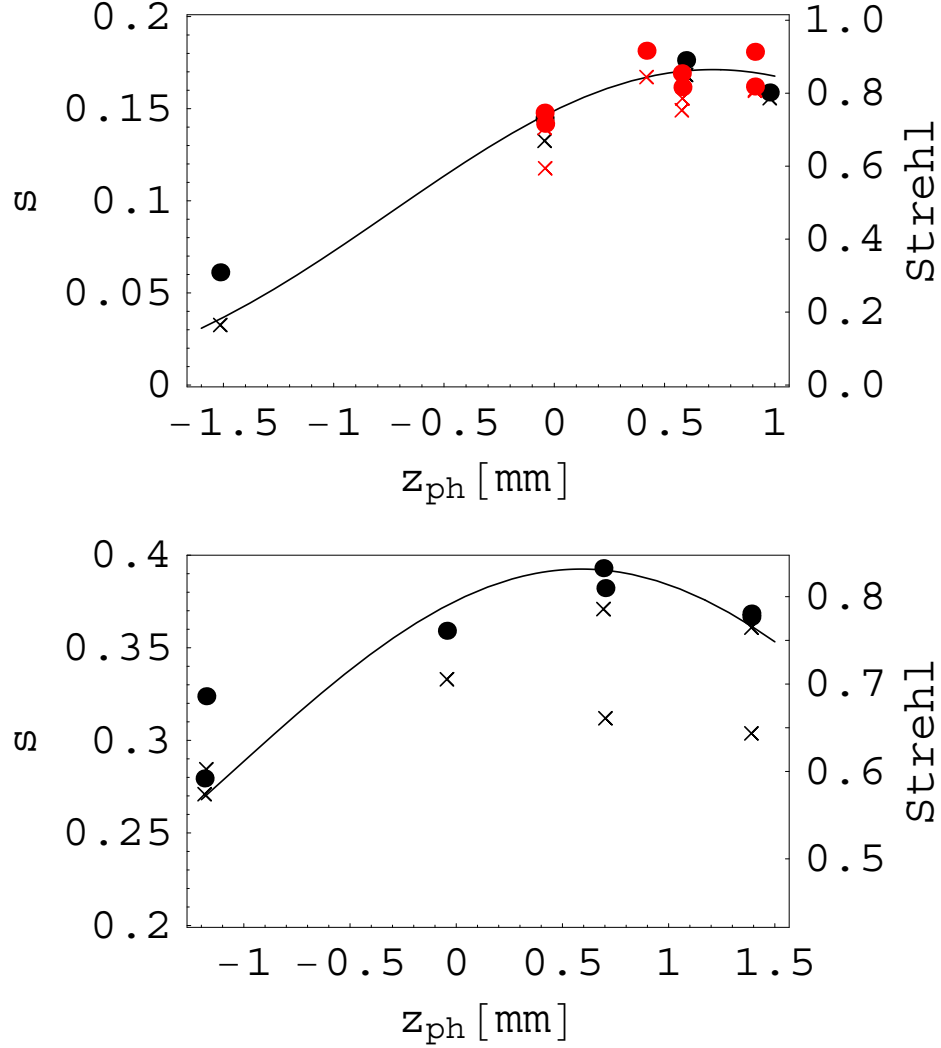
Figure 5: Top: Strehl surrogate s and Strehl *vs.* axial position of the pinhole for the high-res channel for detectors in eye A1 (black) and A2 (red). The data as measured are shown as "ex"s, and the data with the correction for centering are the points. The line is the fit of the data to the central intensity of a diffration image $I(u)$. The focus is at $z_{ph} = 0.72 \pm 0.07\,\text{mm}$, and the RMS residual for s is 0.008. Bottom plot is for the wide-field channel. The line is the fit of the data. The focus is at $z_{ph} = 0.59 \pm 0.06\,\text{mm}$, and the RMS residual is 0.01. For both fits, the correction for centering is used except for the left-most point, because the image is far out of focus and the correction is smaller than the computed value, which is for an in-focus image. Positive means the pinhole is closer to the interior of the instrument.

10

since the average is not so very different from the worst. The fabrication errors of the mirrors reduce the Strehl by 0.96 for the wide-field channel and by 0.92 for the high-res channel. (computed with Maréchal's formula). The optical design reduces the Strehl by an amount that depends on the field position. With the telescope, the range is 0.90–0.99 for the wide-field channel and 0.98–1.00 for the high-res channel. With the pin-hole artificial star, the range is 0.97–1.00 for the wide-field channel. (The telescope has aberrations that the instrument does not fully correct.) On the telescope, the Strehl without atmospheric aberration is expected to be 0.80 for the wide-field channel, which is 4% lower than the value measured with the artificial star.

Case	Meas	Fab err	Design	Expected	Unaccounted
High res	0.86	0.92	0.99	0.91	0.94
Wide field	0.83	0.96	0.99	0.95	0.88
Wide field (on telescope)		0.96	0.95	0.91	

Table 4: Strehl measured at $\lambda 1523$ nm and known factors that lower the Strehl, which are fabrication errors of the optics and the design of the optics.
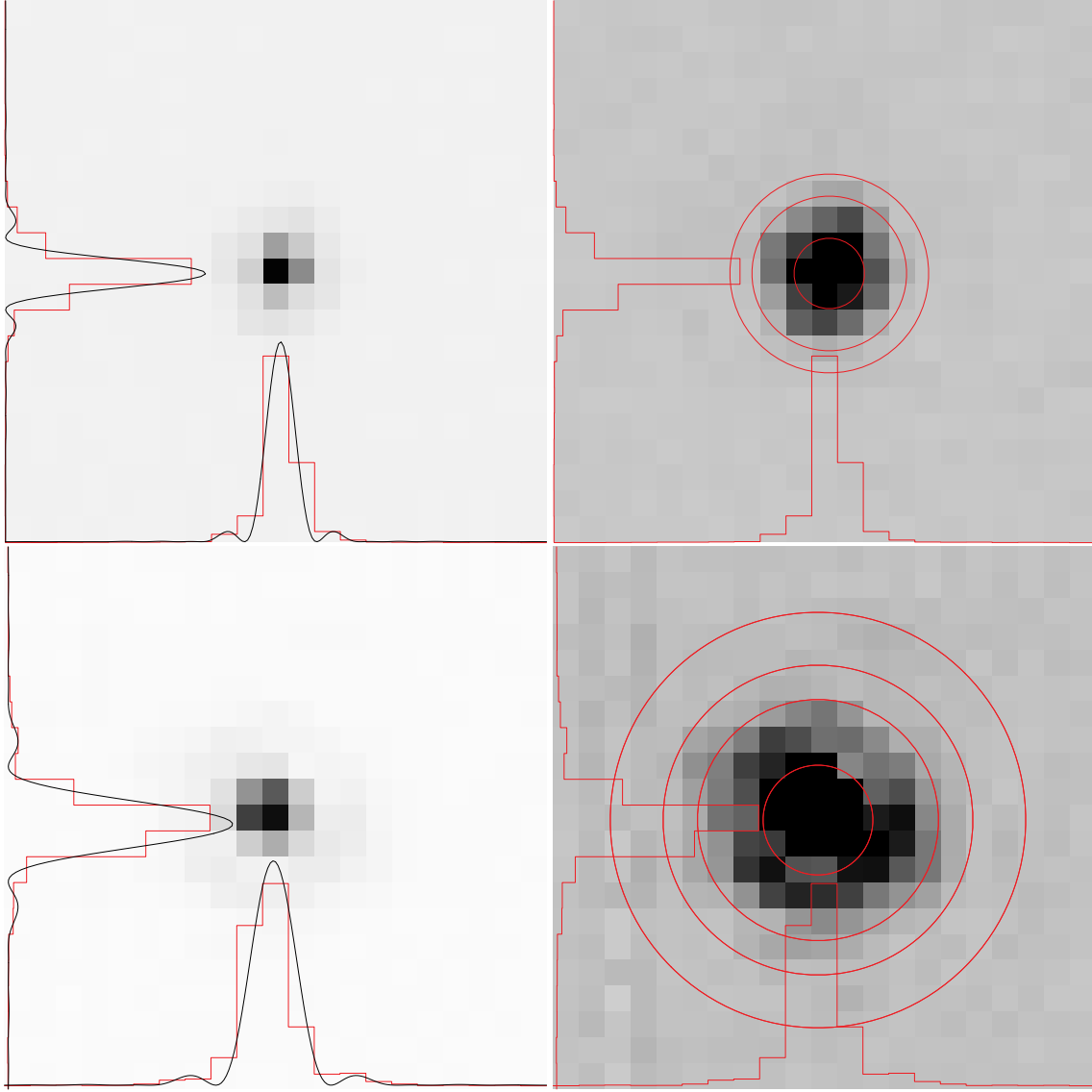
Images of the artificial star are shown in Figure 6.

Figure 6: Image of an artificial star (a pinhole illuminated by a 1.523-μm laser) in the wide-field channel (top panels) and the high-res channel (bottom panels). Horizontal and vertical cuts across the central pixel are shown in red. Cuts of the diffraction image of a circular pupil with a central blockage are shown as continuous lines. On the right panels, the image is printed to show fainter features, and the circles locate the first zeros of the diffraction pattern.
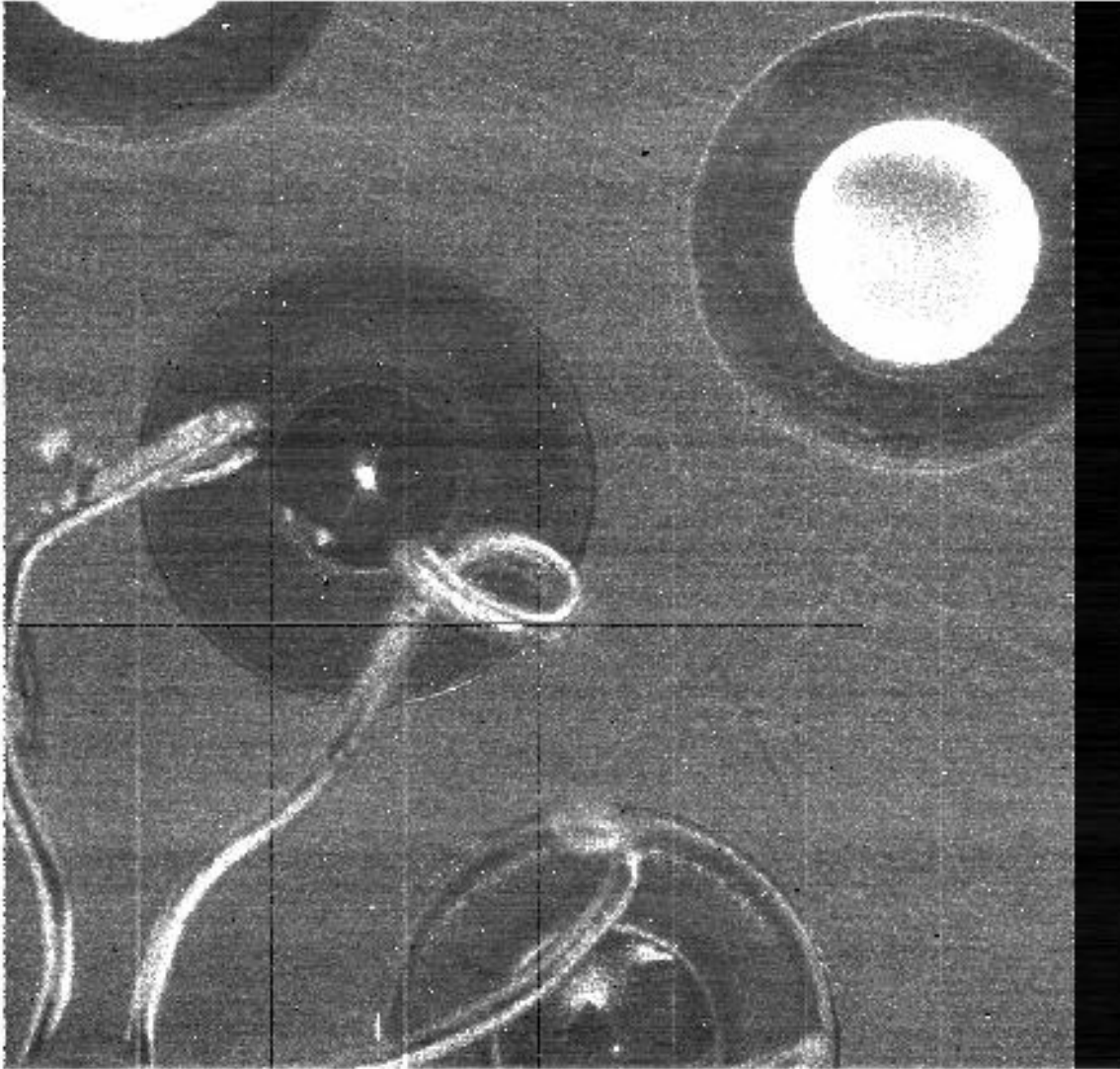
12

Figure 7: Image of the pinholes and the rear of the mask illuminated by laser light that enters unused openings in the mask, which are loosely covered by aluminum foil. The pinhole at the bottom was used for focusing; the pinhole near the middle is saturated. Paper clips bent to shape hold the pinholes.

5 Dark Current and Light Leak

During Run 1, the intensity of images taken with a dark slide blocking the light path was higher than expected;[8] there are two possible causes. First, the temperature of the detector was a few degrees too warm, because half the bolts for the nitrogen reservoir were left off. For this run, that was fixed. The second possibility is a light leak from the vacuum enclosure to the detector. After Run 1, we discovered a light leak. As the detector cables enter the cryo-optical box (COB), they push aside the thermal blanket and allow thermal radiation to enter the COB. We added a second ruffle around the detector cables to cover the opening.
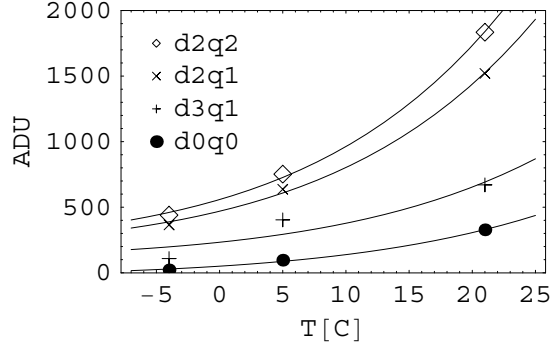

Figure 8: Intensity in a 10-min exposure with a dark slide vs ambient temperature. The points are labeled by detector and quadrant. The line is a fit to the sum of a true dark current, which is independent of the ambient temperature, and a light leak.

We tested for a light leak by measuring the dark current with the instrument in the laboratory and outside in the cold. The intensity of a light leak, which is the integral of the Planck spectrum above the minimum energy of the detector, is approximately

$$I_{\text{leak}}(T) = I_0 e^{-(5750\text{K})/T}.$$

Note $5750\text{ K} = hc/(k2500\text{ nm})$.

The dark current is indeed primarily a light leak. The dark current increases with the ambient temperature, whereas a true dark current depends only on the detector temperature. See Figure 8.

The light leak at 21 C is 0.6 to 2.7 ADU/s, and the true dark current is –0.05 to 0.3 ADU/s, which translates to –0.3 to 1.5 e⁻/s. (See Table 5.) Because the light leak is about 10 times the true dark current, these values for true dark current are uncertain.

The dark current is slightly lower than in Run 1. The detector temperature is 6 C cooler because all of the bolts to the nitrogen reservoir are installed.

---

[8]Baker, D., & Loh, E., 2006, Cold Test #2, Spartan IR Camera

Detector –quadrant	Location	I_{dark} [ADU/s]	$I_{\mathrm{leak}}(21\mathrm{C})$ [ADU/s]	$I_{\mathrm{meas}}(21\mathrm{C})$ [ADU]/s
0–0	Bottom inside	–0.05	0.6	0.5
1–0	Bottom outside			1.9
2–1	Top outside	0.3	2.3	2.5
2–2	Top outside	0.3	2.7	3.1
3–1	Top inside	0.2	1.0	1.1
3–1	Top inside			1.3 Run 1
1–0	Bottom outside			2.4 Run 1

Table 5: Measured intensity I_{meas} and the fit parameters light leak I_{leak} at 21 C and dark current I_{dark}. An ADU is approximately $5\,e^-$. The data from Run 1 are from Baker & Loh 2006.

5.1   Light Leak

We discovered a light leak when we opened the instrument at the end of the run. In the cryo-optical box (COB), there are about twenty ϕ6-mm holes for unused bolts, about twenty ϕ3-mm holes for unused bolts, five ϕ19-mm holes for motor wires, one ϕ19-mm holes for wires for temperature sensors, four ϕ6-mm holes for pins for 4-eye, and 6 ϕ6-mm holes for reference pins. Thermal radiation from the vacuum enclosure can reach the detector by passing through these holes. The radiation through a ϕ19-mm hole 150 mm from the detector is $40{,}000\,e^-/\mathrm{s}$. The multi-layer insulation (MLI) is supposed to prevent 300-K radiation from reaching the COB. The temperature of the radiation between the innermost layer of the MLI and the COB is about 160 K. Because the detector is sensitive only to the short wavelength tail of the Planck spectrum, the radiation at 160 K is negligible.
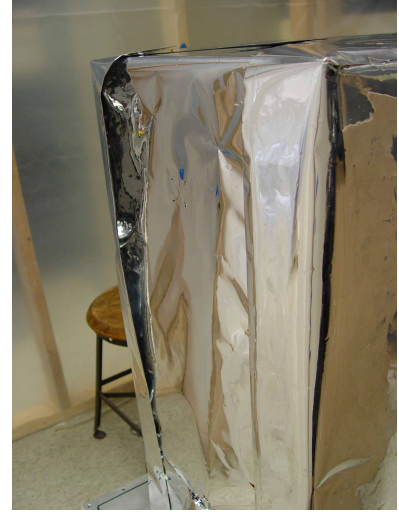

Figure 9: The multi-layer insulating blanket after Run 2 of Cold Test 3. Note that the taping between the bottom and belt of the blanket came undone.

Even though the path from the warm vacuum enclosure to the COB is mostly blocked, there is a possible path. The MLI is made of four sections. Two belts cover the sides of the COB, and the top and bottom sections cover the belts with a 100-mm wide overlap. Tape holds the sections together. When we opened the instrument, we discovered

that the tape between the top and the belt and between the bottom and the belt came undone (Figure 9). Besides opening up a path between the vacuum enclusure and the COB, the separation between the MLI and COB increased to allow radiation to diffuse farther. Radiation may go through the opening, bounce in the region between the MLI and COB, go through the holes in the COB, and reach the detector.

We plan to reduce the light leak in several ways. (1) Use more tape for the MLI to prevent the sections of the MLI from opening up. If that works perfectly, there is no need for the other steps, but we will do them anyway. (2) Put bolts in the unused bolt holes. (3) Put bolts in the unused holes for reference pins. (4) Cover the hole for the wires for the temperature sensors with black aluminum foil. This hole is most likely the biggest problem because there is a direct path between it and the detectors. There is no line-of-sight path between the detector and the other holes for motor wires. (5) Cover with black aluminum foil the holes for the pins for 4-eye.

Detector 0, which has the lowest dark current, is near the inside and bottom of the instrument. (See Table 5.) The detector in channel 1 has a bright corner, which may dominate the dark current. Of the two detectors on the top, the inside one has the lower dark current.

That the detectors on the bottom and on the inside have a lower dark current is consistent with the hole for temperature sensors being the most serious light leak. The detectors on the top see this hole, which is on the bottom, at a more favorable angle. Furthermore, the inside detectors see the hole at a very steep angle.

5.2   Dark Images

The image taken with a dark slide is shown in Figure 10. For comparison, a dark image taken during Run 1 is shown in Figure 11. Surprisingly, the dark current is greater, even though we closed a significant light leak.

Detector 1, Serial #92, has a corner that emits light. The bright corner is in quadrant 1 (counting from 0). See Figure 10. Furthermore, the light appears in the detector at the upper right. The shadow of the pyramid is clear in the image. There is a curved arc for which we have no explanation.
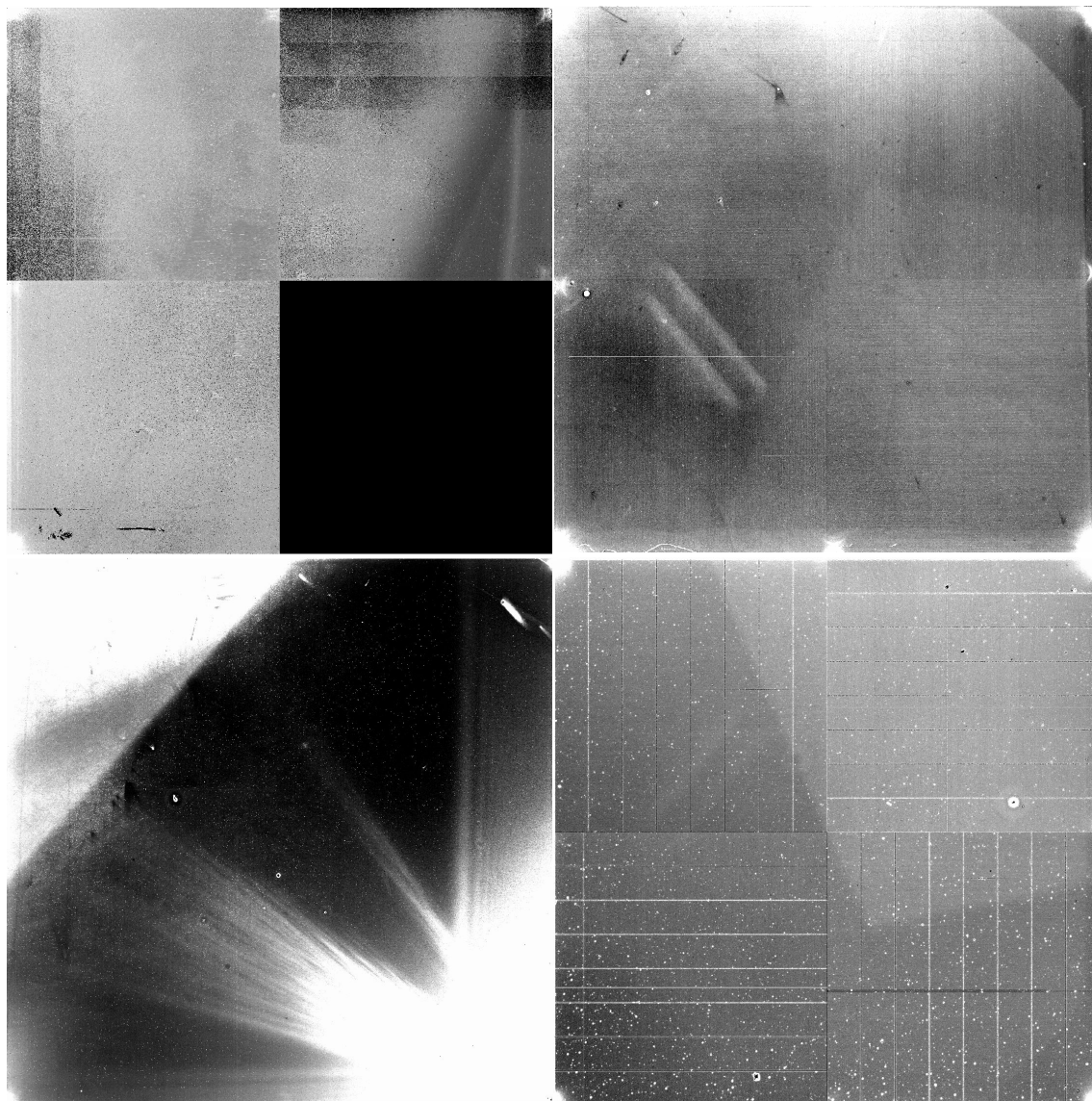
Figure 10: Image taken with a dark slide in the high-res mode during Run 2. The image is printed so that light that reflects off the vicinity of the apex of the pyramid images onto the corners of the figure. To position the 4 sections of the image as if they were pasted onto the surface of the 4 detectors, rotate the four images in this way: For the lower-left detector, rotate the lower-left corner up out of the paper 90° about the axis formed by the lower-right and upper-left corners. For each detector, the outer most corner is raised up.
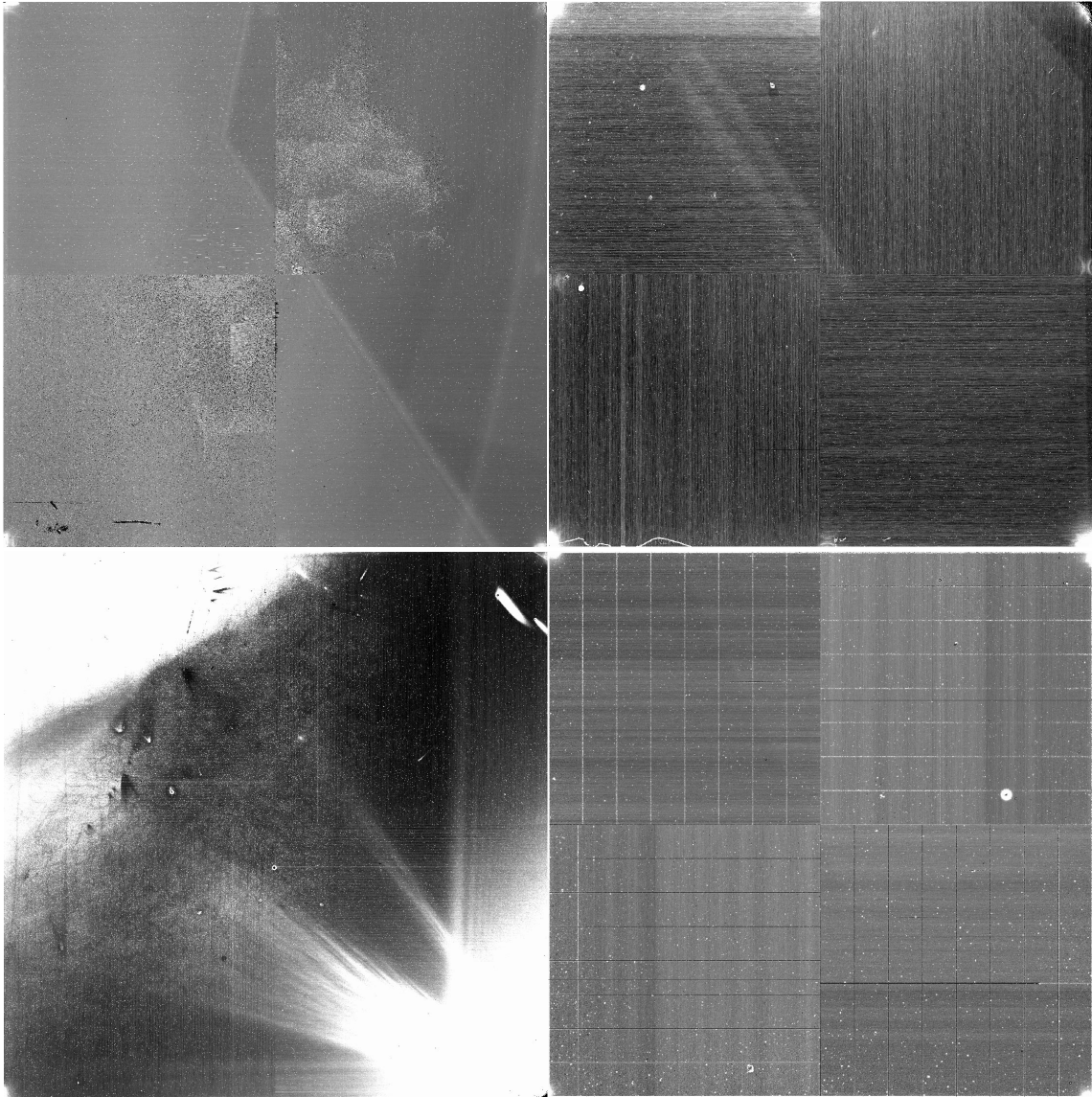
Figure 11: Image taken with a dark slide in the wide-field mode during Run 1

6   Temperature and Pressure

6.1   Partial Warm-up

The temperature and pressure history (Figure 12) of a partial warm up, where the nitrogen was exhausted for 7.6 hr, shows several interesting features.
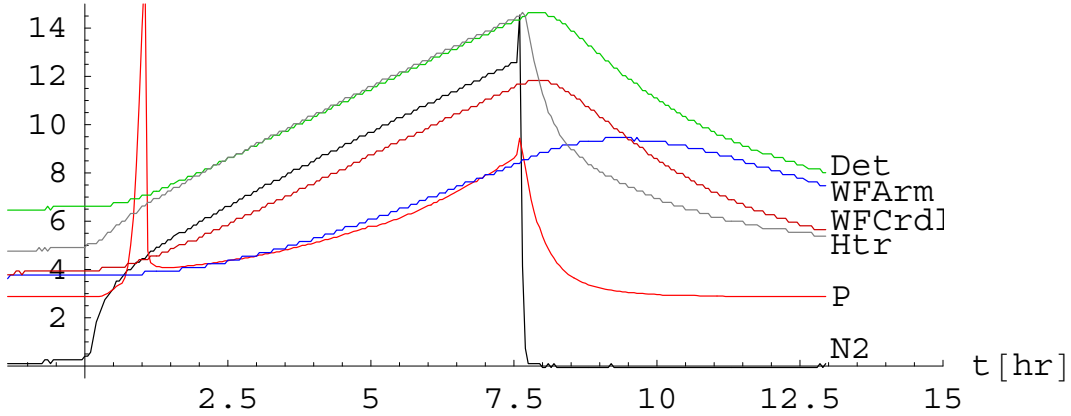
P[μTorr],T-77

Figure 12: Pressure (red) and temperatures of the nitrogen reservoir (black), detector (green), the arm holding the wide-field camera mirror (blue), the cradle of the rotation stage for the wide-field camera mechanism (dark red), and the heater (gray). The temperatures are offset by 77K. The nitrogen was exhausted at $t = 0$ and filled at $t = 7.6$.

The pressure rises sharply 0.7 hr after the nitrogen is exhausted, and it falls again at 1.05 hr even more steeply (Figure 13). During this period of 20 min, the temperature of the nitrogen reservoir rises about 1 C. We cannot explain the momentary rise in pressure during warm-up.

The temperatures of all of the sensors (on the nitrogen reservoir, detector, the arm holding the wide-field camera mirror, the cradle of the rotation stage for the wide-field camera mechanism, and the heater) rise when nitrogen is exhausted, but the temperature of the arm holding the wide-field camera mirror lags, because its heat path is through bearings.

When the nitrogen reservoir is filled, the pressure in the instrument and the temperature of the nitrogen reservoir both rise momentarily (Figure 13). The explanation, we believe, is that warm gas is initially forced into the nitrogen reservoir when liquid nitrogen from the 160-L dewar cools the 1.3-m length of pipe connect-

19

ing it and the instrument. Because the nitrogen reservoir warms, the equilibrium pressure above the charcoal getter rises.
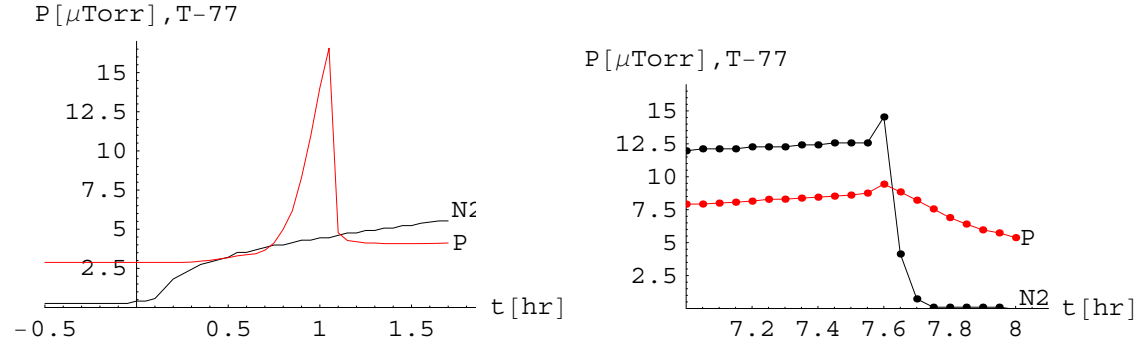

Figure 13: Pressure in the instrument and temperature of the nitrogen reservoir when liquid nitrogen is exhausted (left) and filled (right).

6.2   Temperature of the Mask Wheel

After the mask wheel rotates to or from certain positions, the temperature of the mask wheel changes (Figure 14). The load on the ball bearings of the rotation stage must change with position. If the load is greater, the contact surface is greater, and the thermal resistance decreases.

The temperature change occures only over a certain range of rotation.

After the rotation on day 8.453, the temperature dropped 6 C with an e-fold time of 1.8 hr (Figure 15). With a 6-C change in temperature, the position of a point at the center of the mask wheel shifts 0.46 and 0.28 pixel in the high-res and wide-field modes, respectively.
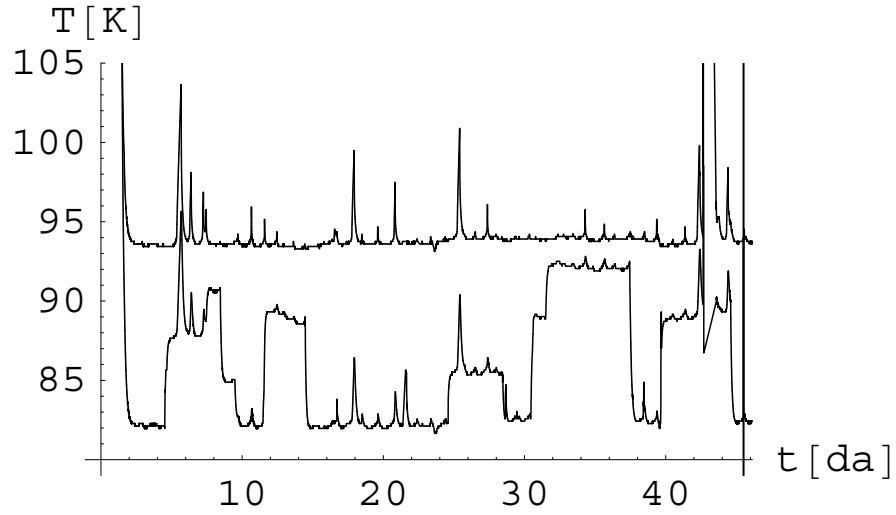
Figure 14: Temperature of the mask wheel (bottom) and the heater (top) offset by 12 C. The wheel was first moved at 3.92 da. A rise in the temperature of the heater indicates the coolant ran out, rather than a change in the thermal resistance of the mask mechanism.
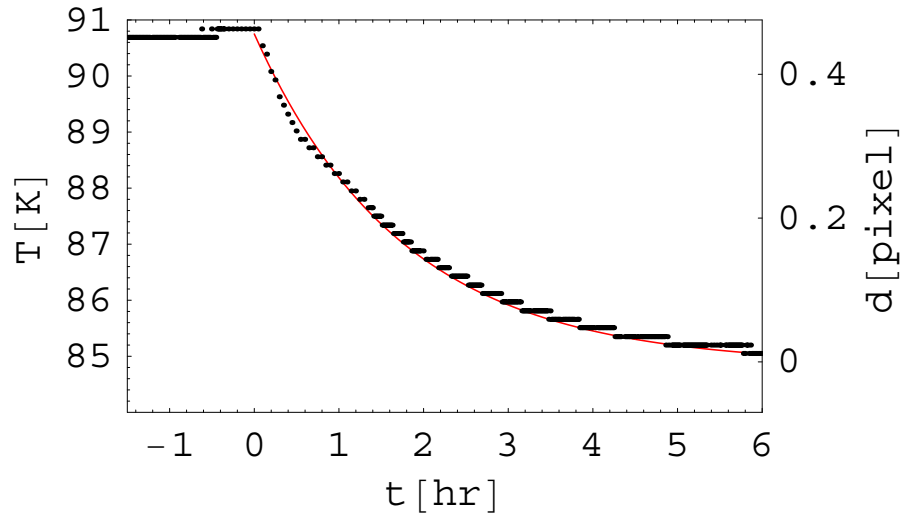

Figure 15: Temperature of the mask wheel after rotating. The line is an exponential with an e-fold time of 1.8 hr. The right-hand axis is the shift in position of the center of the mask in the high-res mode.

7   Hold Time

A 7.5-L load of liquid nitrogen lasts 21 hr when the ambient temperature is 21 C. For this run, the pressure in the instrument is about $5\,\mu$Torr. Since radiation is the dominant heat loss, we expect the hold time to scale with ambient temperature T (in Centigrade) as
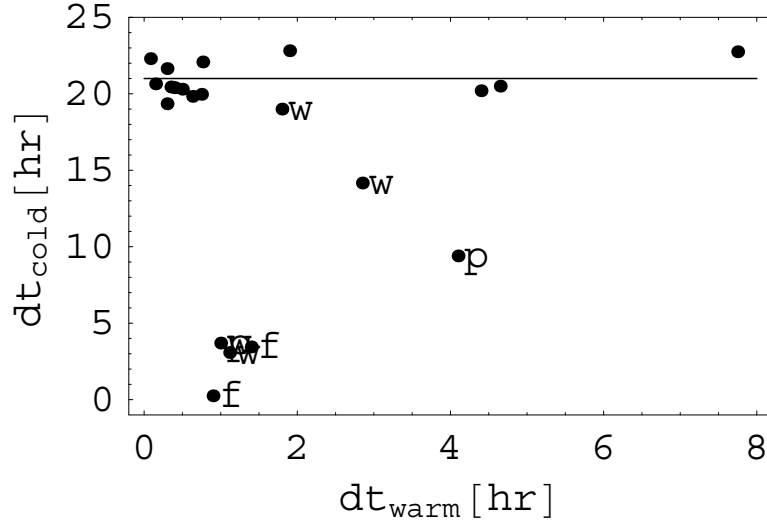
$$t_{\text{hold}}(T) = 28.3 - 0.35T.$$

We found the hold time from the record kept in the instrument log. The time when the instrument was filled with liquid nitrogen can discovered from the temperature of the liquid nitrogen reservoir. The temperature of the liquid nitrogen reservoir rises for two reasons. Of course it rises when liquid nitrogen is exhausted. In addition, the temperature rises if the pressure above the liquid nitrogen rises. When the valve on the 160-L liquid nitrogen dewar is first opened, liquid injected into the warm fill pipes boils rapidly, and the pressure rises for several minutes. The boiling point of nitrogen increases, and during that time, the temperature of the nitrogen reservoir rises. The temperature rise may be 1 C if the initial flow of nitrogen is fast, and it is small if the initial flow is slow.

Define warm duration dt_{w} to be the time during which the temperature of the reservoir is above threshold. We chose the threshold to be 0.2 C above the boiling point at atmospheric temperature. Similarly, define the cold duration dt_{c} to be the time during which the temperature of the reservoir is below threshold.

The lifetime for a load of liquid nitrogen can be extracted from a plot of the warm duration for a filling and the cold duration preceeding the filling (Figure 16). A datum was ignored if the temperature rise is less than 1 C, because the temperature rise is almost certainly because of the increase in the pressure over the liquid nitrogen. Consider the unusual cases, which are culled. In some cases, the temperature of the instrument was not cold at the time of the previous filling. Some of the coolant was used to cool the instrument and not to keep it cold. (These and other data to be culled are marked on the plot.) In a few cases, the reservoir was not completely filled. Finally, the temperature sensor, screwed to one side of the reservoir, is not as cold when the instrument turns. This was the case when we were measuring the flexure.
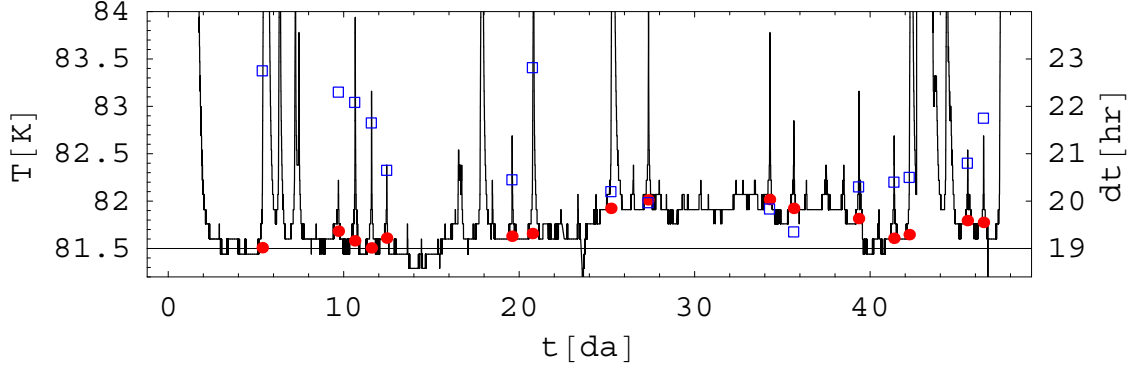
The average of the clean data is 20.9±1.1 hr.

Figure 16: Warm duration dt_{w} vs cold duration dt_{c} for liquid nitrogen fills during Run 2 of Cold Test 3. The cold duration is the time between the previous fill and the rise in temperature. A long warm duration means the instrument warmed up and was not cool again after some time. A "p" marks data for which the previous fill was partial. An "f" marks data for which the instrument was rotated for the flexure test. A "w" marks data for which the wide-field camera arm was warm at the time of the previous fill. (If the instrument was warm, part of the nitrogen is used to cool the instrument.) The line is drawn at 21 hr.

Figure 17: Temperature of the heater *vs.* day with the average temperature over the 18hr preceeding a warm up shown as red points and the cold duration dt shown as blue squares.

7.1 Correction for ambient temperature

The ambient temperature of the laboratory did not stay constant over the run—there was a cold spell where we wore jackets inside the lab, and this affects the hold time. The temperatures of the detector controllers show cooler temperatures at the beginning of the run and a cold spell between days 12 and 24. The range in temperature is 8 C. However, the detector controllers are warmer than ambient, and their temperatures depend on whether their enclosures were mounted with the front and side plates, which changed.

We shall use the temperature of the heater that is mounted on the outside of the cryo-optical box (COB) as a surrogate for the ambient temperature, rather than the temperature of the detector controller. The heater is cooled by contact with the COB, and radiation from the inner-most layer of the insulating blanket warms it. The energy flux of the warming radiation is approximately proportional to T_{amb}^4. Therefore the temperature of the heater depends on the ambient temperature. The temperature variation is only 0.6 where the instrument is cold (Figure 17). The variation is 5 quanta.

The temperature of the heater and the detector controller show the same cold spell between days 12 and 24, but the temperature of the detector controller does not show cooling around day 40. We choose to use temperature of the heater, because it is a more uniform set of data.

The hold time is correlated with the temperature of the heater (Figure 18). As expected, the hold time is shorter when the heater is warmer. The correlation is $\delta dt_{\mathrm{c}}/\delta T_{\mathrm{heater}} = -4 \pm 1$. The hold time is corrected to $T_{\mathrm{heater}} = 81.8\,\mathrm{K}$ by sub-

24
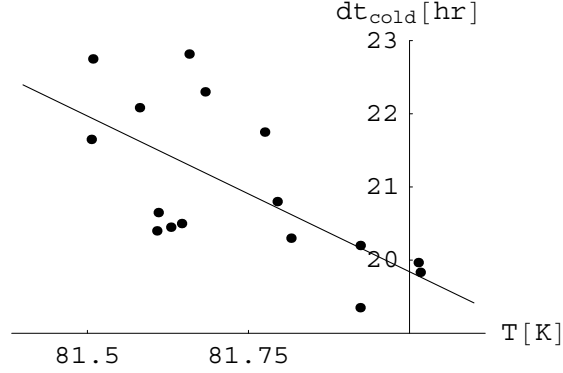
Figure 18: Cold duration dt *vs.* temperature of the heater

tracting the correlation.

7.2   Change over time

There is marginal evidence (Figure 19) that the heat load increased over the course of
the run, but the large scatter indicates some other effect may be more important. For
the uncorrected data, the fit is $dt_\text{C}(t) = (22.1 - (0.042 \pm 0.017)\ t/\text{da})\text{hr}$. For the data
corrected for ambient temperature, the fit is $dt_\text{C}(t) = (22.1 - (0.016 \pm 0.015)\ t/\text{da})\text{hr}$.
The correction reduced the time dependence because the ambient temperature was
cooler during the early part of the run. The corrected data show that the heat load
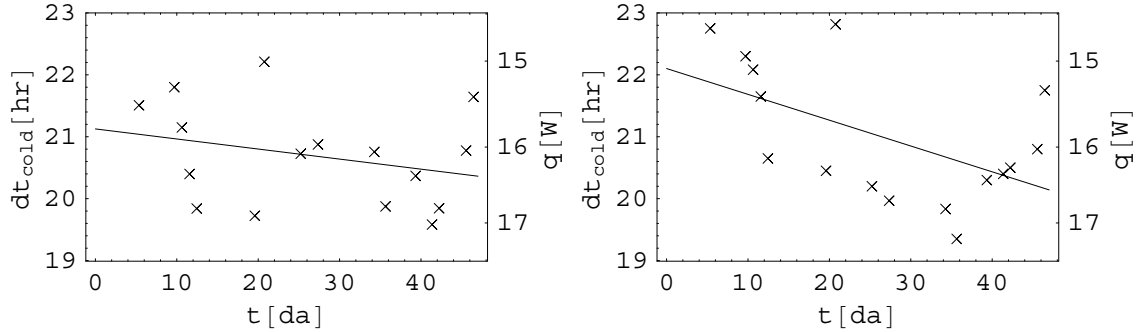increased by $3 \pm 3\%$ over the 46-day run.

Figure 19: Cold duration dt_C and heat load vs time t (corrected for ambient temperature
in the left panel; not corrected in the right panel) since the beginning of the run. The last
two points were taken from the paper notebook, because a temperature sensor failed.

8   Pressure rise

The pressure reading on the ion gauge rises $0.11\,\mu$Torr/day (Figure 20), but the actual pressure depends on the identity of the gas. If the residual gas is 60% He and 40% Ne[9], then the actual pressure rise is $0.54\,\mu$Torr/day. The pressure increases because gas diffuses through the Viton o-rings. The charcoal getter at $77\,$K is able to capture N_2, O_2, CO_2, and Ar, but not He and Ne. On the ion gauge, the pressure reading is a factor of 5.9 and 4.1 lower than the actual pressure for He and Ne respectively.[10]

Over the course of a year, the pressure rises to $0.2\,$mTorr. The molecular conduction[11] at that pressure is $2.8\,$W, which is acceptable compared with the heat load of $16\,$W. The dominant molecular conduction is between the walls of the vacuum enclosure and the cryo-optical box. The 10-layer thermal blanket interrupts the conduction, and reduces it by a factor of 10.
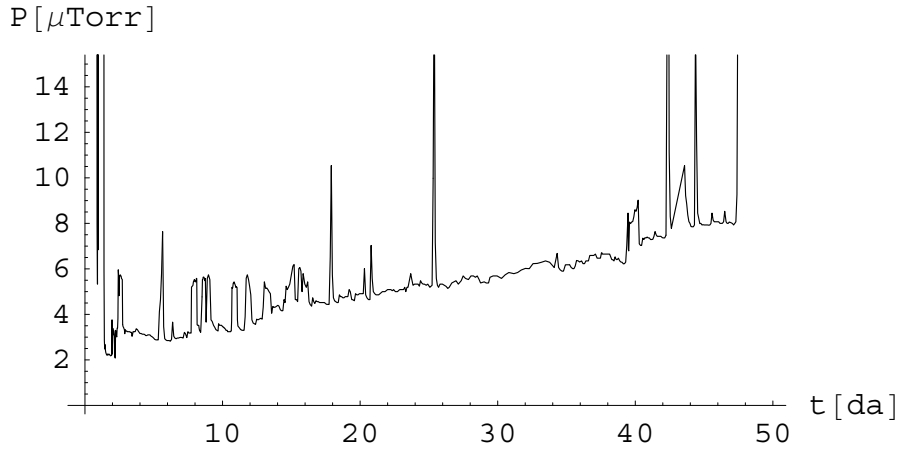

Figure 20: Pressure during Run 2 of Cold Test 3 since 00:00 on 1/22/2007, which is day 0. The pressure was erratic at the beginning; the pressure jumped to about $5.5\,\mu$Torr. The pressure gauge was degassed at 16:45 on day 15 and a few times after that. The pressure became stable after 05:00 on day 16. The events with high pressure are due to exhaustion of liquid nitrogen.

---

[9]Loh, E., 2003, unpublished.

[10]Inficon, undated, BPG400 Operating Manual, p. 51.

[11]The molecular conduction is $q = (\gamma+1)Pv/(8(\gamma-1)T)$, where γ is the ratio of heat capacities, v is RMS speed, and T is temperature. (O'Hanlon, John F., 1980, A User's Guide to Vacuum Technology, Wiley, New York.) For air $q = 0.15(P/1\mu\text{Torr})(290\text{K}/T)\text{mW/K/m}^2$.

9   Noise

9.1   Filters for the controller

The power spectrum[12] of a row of a quadrant shows an excess noise at low frequency. (See Figure 21.) This is not surprising, since the circuit on the detector is almost DC-coupled. Once a row, the controller samples a pixel that has no charge. Therefore the referencing frequency is 1/1024 that of the pixel frequency. The power spectrum is measured for the difference between two long–short images taken with the same conditions, in order to remove the pixel-to-pixel variations due to fixed-pattern noise, defects, and dark current.

The white noise for detector #74 in channel 2 is high, and a possible reason may be a problem with this detector. Pixels are shorted together, and the image does not look clean: the shorted pixels are still apparent in the difference between two images.

Ideally, the noise in each pixel is independent of that in any other pixel, and the noise spectrum should be white, independent of frequency. For detector 2, the noise at frequency $f > 0.03\,\text{pixel}^{-1}$ is white. For the other detectors, there is an upturn at high frequency. That upturn depends on the value of bias gate and the offset that is subtracted from the signal. More work is needed to track that down.

We found that filtering the 5-V regulator on the controller board reduced the noise at low frequencies and filtering the 2.5-V reference reduced an oscillation. To test filtering, we put the 5-V power on a resistor divider on the input in place of the detector. The resistor divider puts the 5V in range of the signal chain and makes the impedance 3kΩ, which is approximately the same as the output impedance of the detector. There is low-frequency noise and an oscillation at $0.02\,\text{pixel}^{-1}$ or $2.8\,\text{kHz}$. Filtering the 2.5-V reference reduces the amplitude and frequency of the oscillation, both scaling as $C^{-0.6}$, where C is the filter capacitance. We put an additional $440\,\mu\text{F}$ on the 5-V regulator and on the 2.5-V reference. The capacitors are Vishay-Sprague 10-V, $220\,\mu\text{F}$ tantalum capacitors (594D227X9010D2T).

The noise spectra (Figure 21) of the cold detectors show that the additional filters decrease the noise in the frequency range between 0.005 and $0.05\,\text{pixel}^{-1}$.

---

[12]Used here, the spectrum is the root-mean-power in a bin: For white noise of unit variance, the root-mean power is $\sqrt{2}$ for every bin. For a sinusoidal, the root-mean power is $\sqrt{(2/n)}$ in one bin and zero in all others, where n is the number of data in the original data and $n/2$ is the number of data in the spectrum.
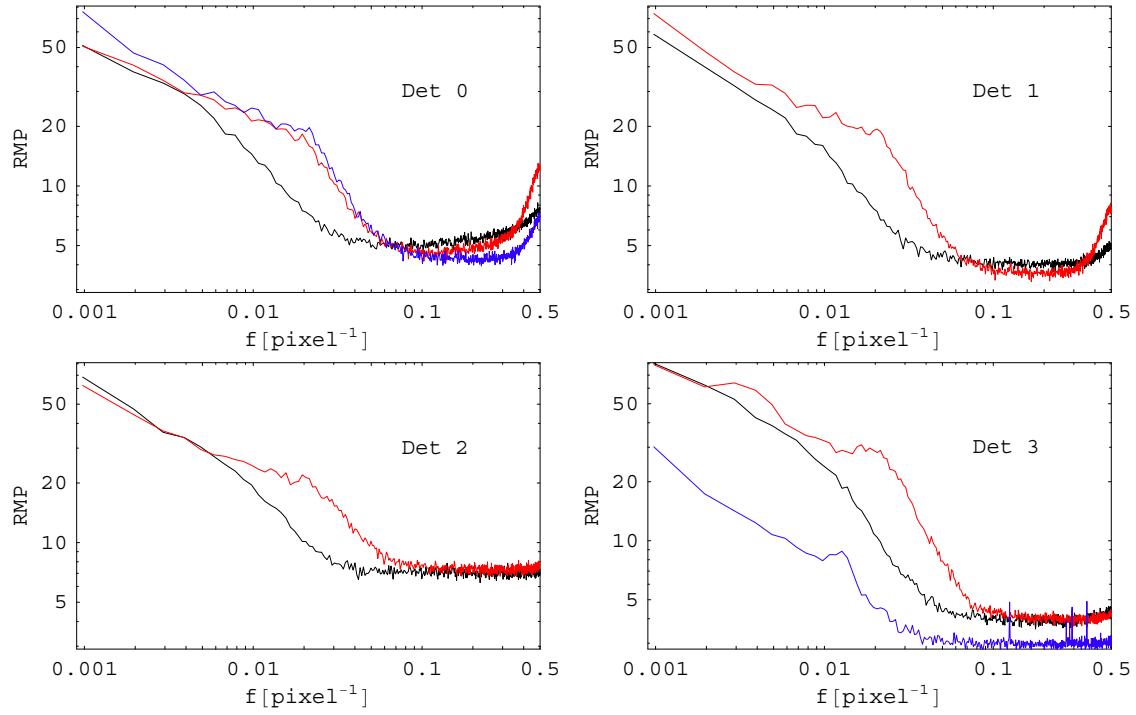
Figure 21: Noise spectra of the long-short images for each detector with new (black) and old (red) set of filters on the controller. For detector 0, shown in blue is the spectrum with the old filter and a different offset voltage. For detector 3, the noise spectrum with a 2.5-kΩ load (no detector) is shown in blue.

9.2 Photon and detector noise

To calibrate the system in $\mu V/e^-$ and to measure the noise of the system, we took a set of pictures of a sheet of paper lit by an incandescent lamp, which approximates a uniformly illuminated field, at differing exposure times and also pictures with a dark slide. At each exposure time, three pictures were taken. The first was not used, since the detector has a memory.[13]

For the i-th pixel of the picture j, the variance is a linear function of the mean, since the variance is the sum of a light-independent term, v_0, and photon noise, which depends on the mean $m_{j,i}$.

$$\operatorname{var} p_{j,i} = v_0 + a m_{j,i}.$$

We estimate the variance in two ways. For the pictures with the dark slide, we analyze the difference

$$d_i = (p_{1,i} - p_{2,i})/\sqrt{2}$$

between two pictures $p_{1,i}$ and $p_{2,i}$ The variance of the i-th pixel is $\operatorname{var} d_i = (p_{1,i} - p_{2,i} - m_{1,i} + m_{2,i})^2/2$. Since the amount of light is slight, $m_{1,i} + m_{2,i}$ is nearly independent of pixel. Then

$$\operatorname{var} d_i \approx (p_{1,i} - p_{2,i} - M)^2/2,$$

where $M = \langle p_{1,i} - p_{2,i} \rangle$ is the average across the picture. The average variance

$$\operatorname{var} d = \langle \operatorname{var} d_i \rangle \approx \left\langle (p_{1,i} - p_{2,i} - M)^2/2 \right\rangle.$$

To remove defects, pixels that are 5 standard deviations from the mean are removed from d.

We choose to compute the variance in transform space, in order to isolate the low-frequency noise. The noise at low-frequencies of these detectors is poor, because the signal is almost DC-coupled. The electronics are referenced once per row: the reference frequency is 1/1024-th of the signal frequency. Let $\hat{d}_k$ be the Fourier transform of $(p_{1,i} - p_{2,i} - M)/\sqrt{2}$. Because of Parseval's Theorem, the averages in transform space and in real space are the same.

$$\operatorname{var} d \approx \left\langle (p_{1,i} - p_{2,i} - M)^2/2 \right\rangle = \left\langle \hat{d}_k \right\rangle.$$

To eliminate the very low frequencies, the lowest 8 points (of 1024) are dropped in the average in transform space.

---

[13]Baker, D., & Loh, E., 2006, Cold Test #2, Spartan IR Camera

With the model of photon noise and light-independent noise, $\operatorname{var} d_i = v_0 + a(m_{1,i} + m_{2,i})/2$, where $m_{j,i}$ is the mean of the i-th pixel of picture j, and averaging across the picture yields

$$\operatorname{var} d = v_0 + a(m_1 + m_2)/2.$$

Thus a plot of $\operatorname{var} d$ vs. $(m_1 + m_2)/2$ is a straight line.

For other pictures where there is a significant amount of light, the two pictures $p_{1,i}$ and $p_{2,i}$ do not have the same amount of light because the light source or dark current are not perfectly constant. We analyze the picture

$$d_i = (p_{1,i} - m_1/m_2 p_{2,i})/\sqrt{2}.$$

The variance $\operatorname{var} d = v_0 + a(m_1 + m_1^2/m_2)/2 + ((m_1/m_2)^2 + 1)v_0/2$. For these data, we fit the left hand side of

$$\operatorname{var} d - ((m_1/m_2)^2 - 1)v_0/2 = v_0 + a(m_1 + m_1^2/m_2)/2$$

with $(m_1 + m_1^2/m_2)/2$ as the independent variable. (Since the correction depends on v_0, the fit must be done interatively.)

The data for three detectors, linear fits, and residuals are shown in Figure 22. (The fourth detector, #74, was not analyzed because a fraction of its pixels are shorted together.) The units are counts of the analog-to-digital converter (ADC). The error is $2/(N_r N_s)^{1/2} \operatorname{var} d$, where N_r is the number of rows and N_s is the number of points in the noise spectrum.

The calibration of the system output to photoelectrons and the noise in the absence of light are derived from a fit of the data. If the system measured electrons rather than counts of the analog-to-digital converter, the slope would be unity. The results are in Table 6. The detector controller converts $12.7\,\mu\text{V}$ at its input to a quantum of the analog-to-digital converter, an ADU. The noise of a long–short image[14] in the absence of light (last two columns of the table) is a measure of the noise that the FET on the detector and the controller electronics introduce.

9.2.1   Saturation

The data for which the average intensity is 25,000 has a variance that is a factor of 4 too high (top panel of Figure 23), and we believe that saturation is the cause. The histograms (Figure 23) show the distribution of intensities for 128-column wide

---

[14]The long picture is taken after an exposure; each row in the short one is read immediately after removing the charge. Although the noise in a pixel of each picture is $\frac{1}{2}kT$, the difference is free of that noise.
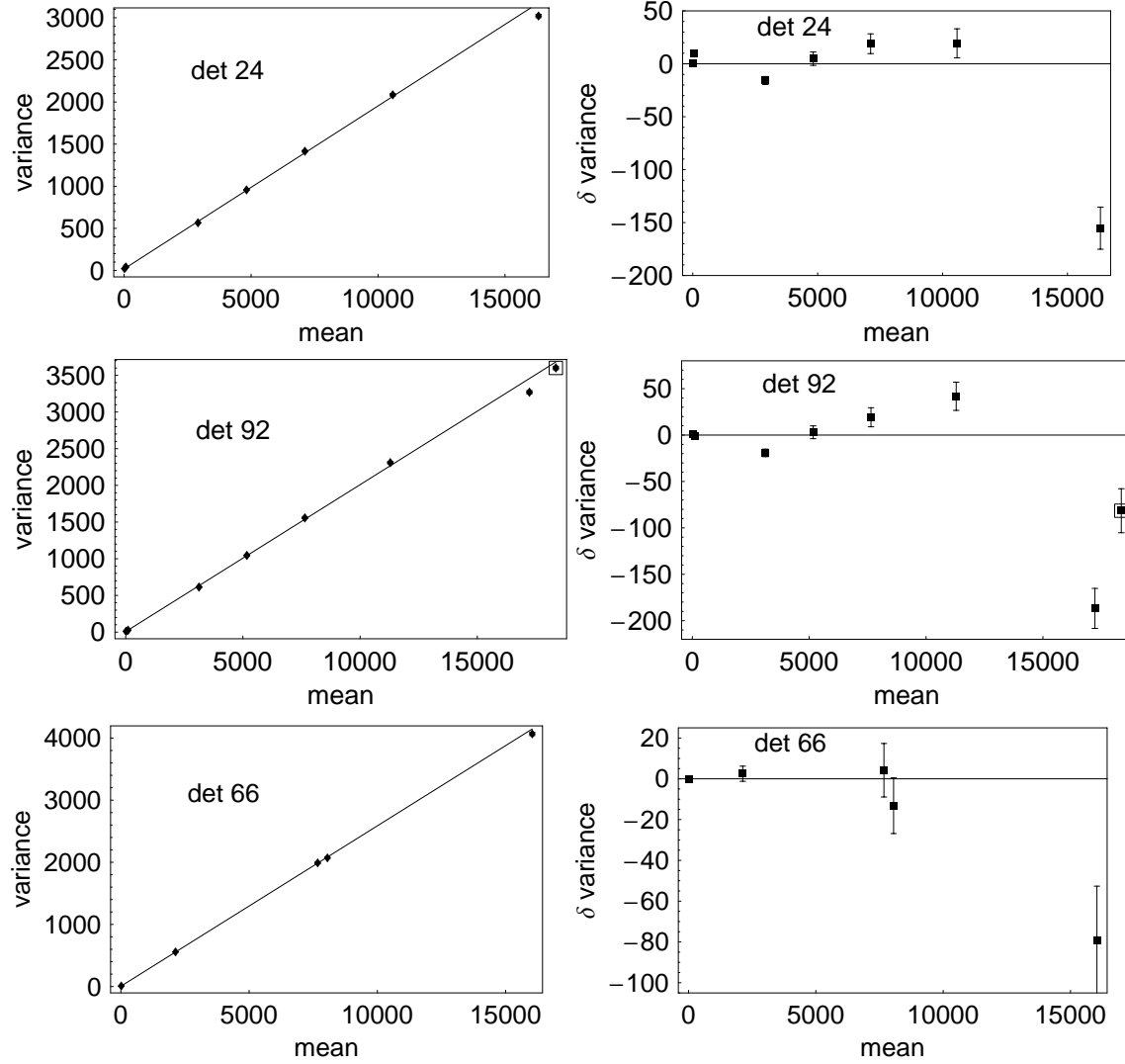
Figure 22: Left panels: Mean *v.s.* variance of the central 200 rows of quadrant 0 for three detectors. The line is a fit to the model with photon noise and a light-independent component. The point around 15000 is not included in the fit. Right panels: Residuals of the fit.

Detector	a^{-1} or a			$v_0^{1/2}$	
	[e$^-$/ADU]	[μV/e$^-$]	[fF]	[ADU]	[e$^-$]
(1)	(2)	(3)	(4)	(5)	(6)
#24 in chan 0	5.14 ± 0.09	2.48 ± 0.04	$65. \pm 1.$	4.8 ± 0.2	$25. \pm 1.$
#92 in chan 1	5.04 ± 0.11	2.52 ± 0.06	$63. \pm 1.$	1.7 ± 0.8	9 ± 4
#66 in chan 3	4.07 ± 0.02	3.13 ± 0.01	51.2 ± 0.2	2.2 ± 0.1	9.1 ± 0.5

Table 6: Detector parameters. Column 2 refers to the output of the system; columns 3–4 refer to the signal at the output of the detector. The noise of a long–short image with no light is in columns 5–6.

segments. For the point with an average intensity of 17,000, both the variance and the histograms are reasonable. For the points with an average intensity of 25,000, the shapes of the histograms (two lower panels in the figure) are far from gaussian. For detector 24, the histogram for right most segment (in red) is a gaussian with a tail. As the segment moves to the left, the tail grows, and a sharp cut-off at 24,900 becomes more prominent.
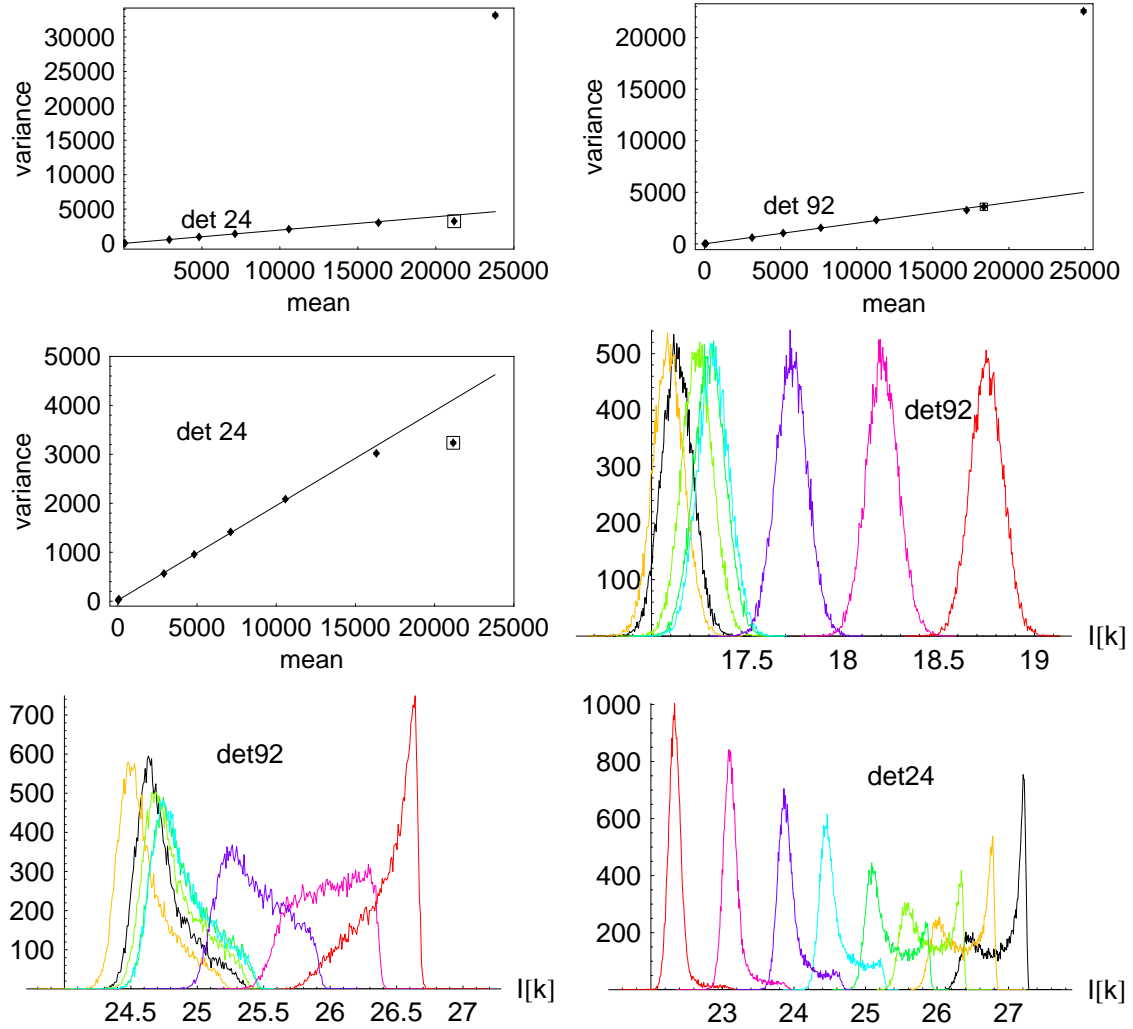
Figure 23: Top: Median *v.s.* variance of the central 200 rows of quadrant 0 for detectors 24 and 92 with the datum at the highest intensity included. The boxed datum was measured from the histogram of the right-most segment of detector 24. Other panels: Histograms of the central 200 rows separated into 128-column-wide segments. The intensity, in kilo ADU, is shifted to the mean intensity of the segment of the original picture. The hue changes from black, orange, green, blue, to red as the segment center goes from column 64 to column 960.

33

10   Flexure

The test is to measure the flexure of the instrument as the direction of gravity changes. Mounted at the Nasmyth position, the Spartan Camera turns about one axis as the telescope tracks a star. For the flexure test, a pinhole on the mask, which is at the focus of the telescope, is imaged on the detector. Thermal radiation emitted by paper covering the window illuminates the pinhole. The flexure test does not reveal flexure of the vacuum enclosure and the A-struts, because the shift between the pinhole and the outside is not measured. The calculated shift due to the A-struts has an amplitude of $9\,\mu$m at the mask wheel, which is 0.4 and 0.7 pixel for the wide-filed and high-res channels, respectively.

We measured the shift of the image of the pinhole (Figure 24) as a function of the orientation of the instrument. The light enters from above at the 0-degree orientation. The first two measurements were ignored.
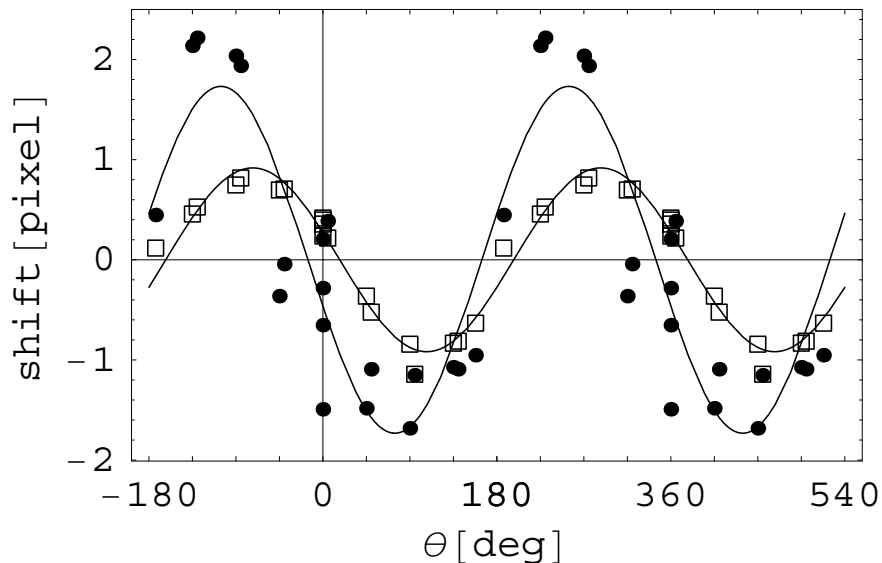

Figure 24: Top–Shift in direction of symmetry (box) and in perpendicular direction (points) vs intrument orientation for the high-res channel at 77K.

The measurements of flexure here are worse than those of Cold Test 2.[15] For the high-res channel, the RMS residual in the direction in which the instrument is not symmetric, 0.6 pixel, is much larger than that found during Cold Test 2 for the wide-field channel (0.07 pixel).

---

[15]Baker, D., & Loh, E., 2006, Cold Test 2, Spartan IR Camera for the SOAR Telescope.

There is a large drift for the wide-field channel (Figure 25). The shift in the non-symmetric direction is 30 pixel, whereas the amplitude of the shift due to flexure is about 2 pixel. A single large shift of 17 pixel occurred with the high-res mode.
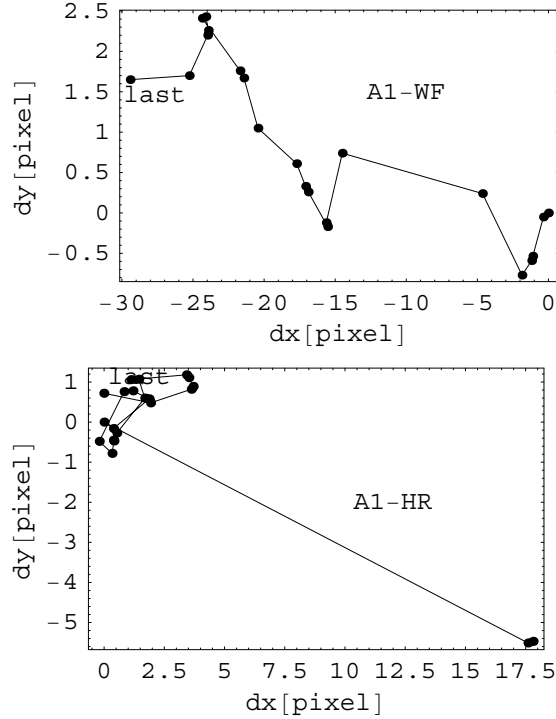

Figure 25: Position of the image for the flexure measurements for A1 in the wide-field (top) and high-res (bottom) modes. The y-direction is the direction in which the instrument, except for the 4-eye detector assembly, is symmetric.

For the high-res mode, the single large shift was the same for all three functioning detectors. For the wide-field mode, the shift was the same for two detectors for the few cases that we checked.

The image size changes monotonically for the wide-field measurements but not for the high-res measurements (Figure 26). This is the crucial observation.

The temperature inside the instrument was stable during the flexure measurements (Figure 27). The temperature changes account for extremely small shifts in the image location. For example, with a 1-C change in the temperature of the mask wheel, thermal expansion causes the image to shift by 0.08 and 0.05 pixel in the high-res and wide-field modes, respectively.

We believe the 4-eye detector assembly is the problem. When changing between
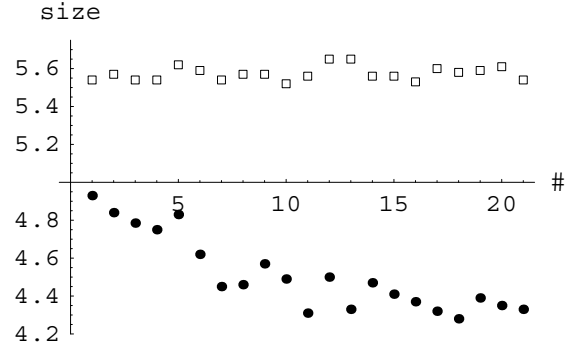
Figure 26: Image size vs measurement ordinal for the flexure measurements in the high-res (box) and wide-field (point) modes. The image size is twice the RMS.

the wide-field and high-res modes, the detectors rotate 9°. The mechanism moves between two stops. If the mechanism does not reach the stops, the focus will be off. We believe the mechanism is not hitting the stops. There is little else that can change the focus and therefore the image size. The fact that the shift is the same for more than one detector is a surprise. Initially we interpreted that to indicate that the cause was not in the 4-eye detector assembly. What that really means is that a single cause makes all of the detectors not seat.
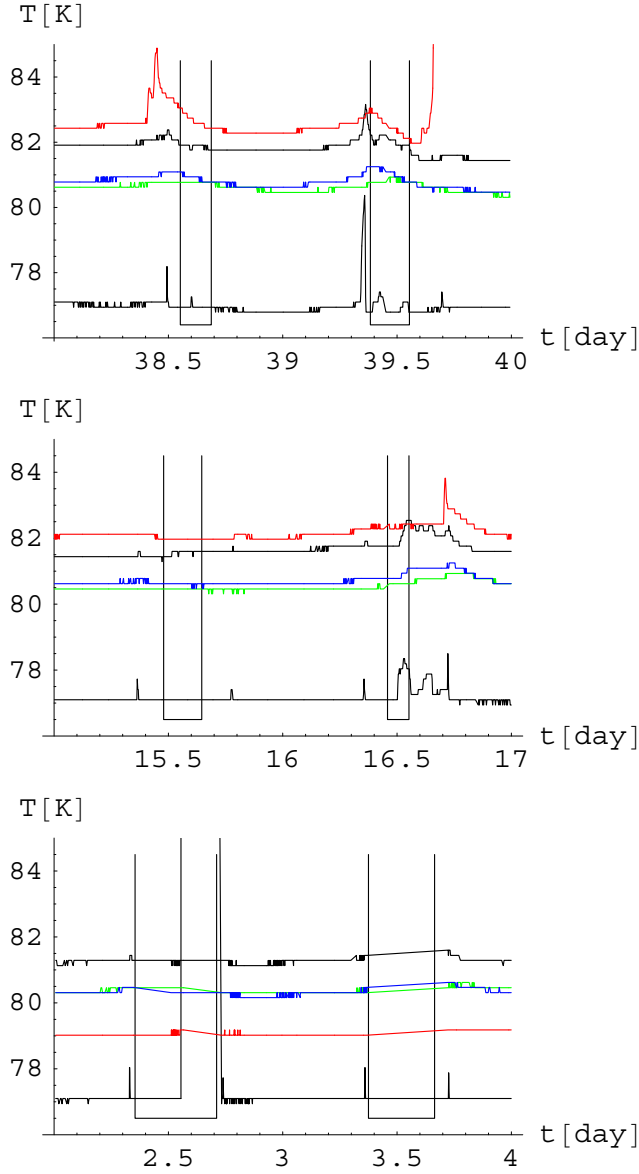
Figure 27: Temperature of the nitogen reservoir (black), heater (black), mask wheel (red), wide-field cradle (blue), and the wide-field camera arm (green) vs day during flexure measurements for the wide-field (top) and high-res (middle) channels. The period over which the measurements were made are marked; for example, flexure measurements for the wide-field channel were taken during the intervals around 38.6 and 39.5. For comparison, the bottom panel shows temperatures (Here the red line is for the high-res cradle.) during the flexure measurements of Cold Test 2.

37

11 Linearity

To measure the linearity of the detector and electronics, images of an artificial star were taken with varying exposure times. The light source was a piece of paper taped to the window. There was no filter.

With the 308-s exposure, the intensity in the central pixel of the image is 27 kADU, which is saturated. For the 128-s exposure, the intensity in the central pixel of the image is 17 kADU.

The data fit a line well, and the residual to the fit shows no evidence of nonlinearity (top panel of Figure 28). The intensity of the light source drifts with time (middle panel of Figure 28). The source was low by 2% at the beginning and again at 0.7 hr.

The fit with the low points at the begining and at 0.7 hr dropped shows (bottom panel of Figure 28) that the data are linear to 1%.

In summary, for an artificial star where the intensity of the central pixel is less than 17 kADU, the system is linear to 1%. The measurement is limited by drift in the light source.
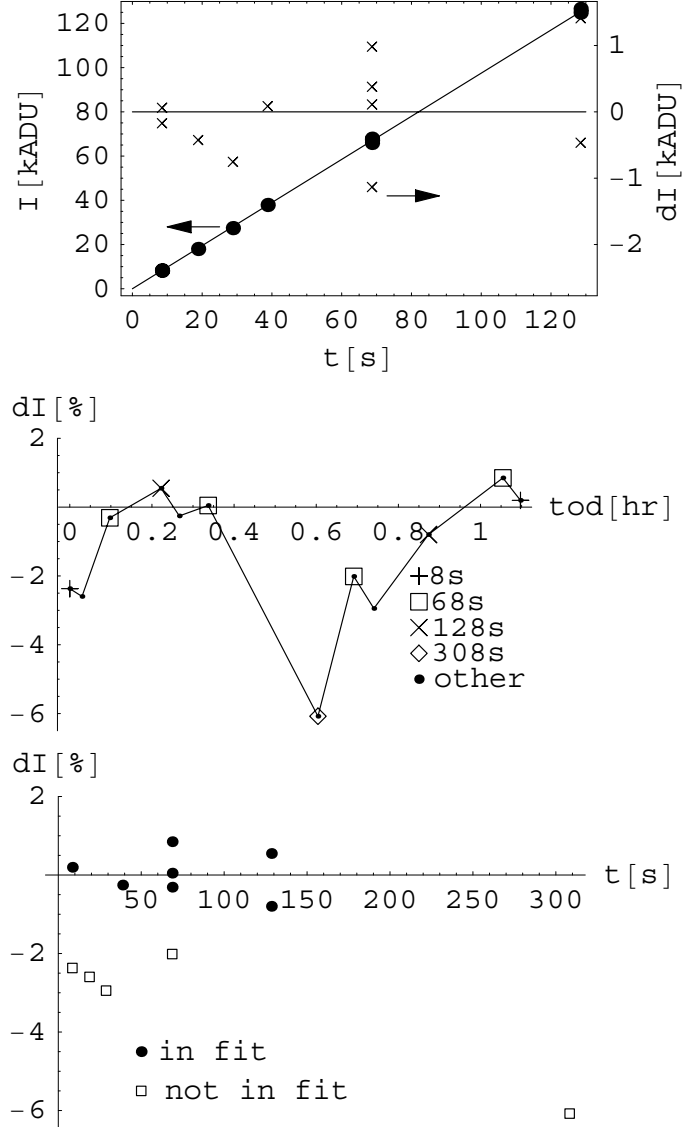

Figure 28: Top—Intensity of an artificial star *vs.* exposure time and residual of the fit to a straight line. A saturated point at 308 s is not included in the fit. Middle—Residuals *vs.* time of day. Bottom—Residuals *vs.* exposure time, fitting selected data.

38

12   Electronic drift

The signal chain is DC coupled, and that is an ill omen. Two features alleviate this problem. In the detector controller, a circuit subtracts the so-called offset voltage from the input signal before amplification. The offset voltage must be set before the image is read out. A reference pixel, which is not light sensitive, is read many times at the end of each row, and the average intensity of the reference pixel is subtracted from each pixel. This is done in software.

The output of the electronics changes over time. Figure 29 shows the average intensity of the reference pixels over a two-day set of measurements of the flexure of the instrument. During that time, the instrument turned, and the temperature of the detector controller changed. The airflow on the detector controller changes with the instrument orientation.

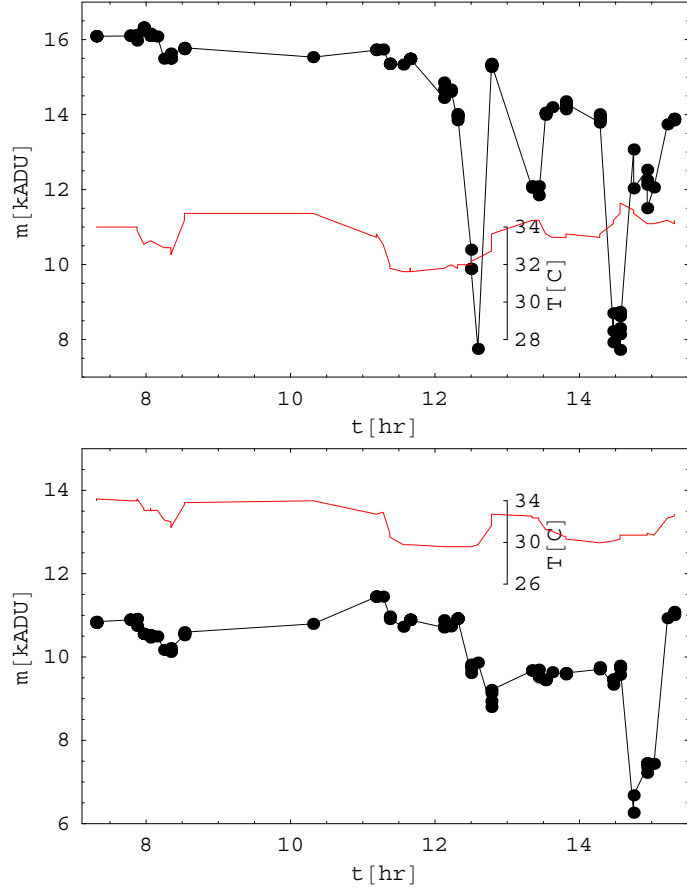The output level makes large jumps. For channel 0, the jumps occurred at 12:30 and 14:45.

Figure 29: Mean intensity of the reference pixels (black) and controller temperature (red line) vs time for channel 1 (top and channel 0 (bottom). The data taken before 11:00 were actually taken 16 hours earlier; they have been moved to condense the plot.

For channel 0, the drift in the output is correlated with the temperature of the detector controller. See the upper panel in Figure 29. The drop in temperature at 8:00 and at 11:20 match the drops in the intensity. The correlation is $290\pm20\,\mathrm{ADU/C}$ for the first day. For channel 1, the output is not correlated with temperature, the correlation being $-20\pm90\,\mathrm{ADU/C}$. For channel 3, the correlation is $43\pm9\,\mathrm{ADU/C}$

39

for the first day.

The drift of several thousands of ADU is a serious problem, since the circuit may bottom out or saturate. This problem has a undesirable effect for observers. The observer must watch for the drift and correct for it.

12.1   4-V reference

The Analog Devices ADR434 4.096-V reference, which the offset circuit uses, is the cause for the drift. At the 5.6-mA operating current, this part needs at least $1.7\,\mathrm{V}$ between its input and output (called headroom). The actual headroom is insufficient, since the measured output is low by $100\,\mathrm{mV}$, whereas the output should be accurate to $5\,\mathrm{mV}$. Therefore the voltage reference, rather than isolating the power, is passing variations in the power to the offset voltage. A small change in the voltage of the power supply is magnified in the image: If the power supply changes by $13\,\mathrm{mV}$, the signal level changes by 1000 ADU.

We replaced the ADR434 reference with an ADR444 which has a headroom of $0.5\,\mathrm{V}$. We have not seen large changes in the images, and the drift of a test signal is about 150 ADU, when the temperature of the detector controller changes $50\,\mathrm{C}$.[16] We measured the drift with the test signals, 5V, biasGate, vReset, and a 3-kΩ resistor. The first three signals are divided by 2, 1.5, and 1.2, respectively. See Figure 30. The detector controller is put in a thermoelectric heater/cooler.
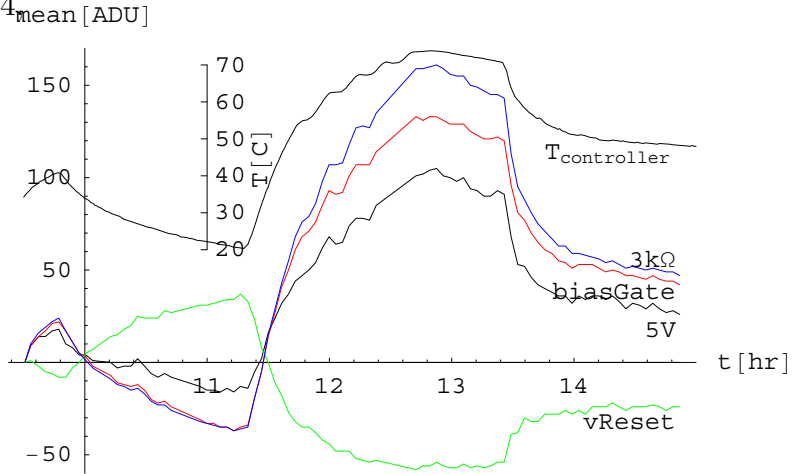

Figure 30: Mean of the short image of test signals *vs.* time of day. The test signals, biasGate, VDDA (+5V), vReset, and a 3-kΩ resistor, are put on the detector card. An ADU is $13\,\mu\mathrm{V}$ at the input of the controller card. The temperature of the controller card is shown too.

---

[16]Loh, E., 2007, Electronics for the Spartan IR Camera, in preparation

With the new 4-V reference, the drift in the output is no longer large and unpredictable. There is a small sensitivity to the temperature of the detector controller. A change of 150 ADU, which is 1/400th of the range of the analog-to-digital converter, occurs if the ambient temperature changes by 50 C. This is acceptable.

12.2 Warm up of a detector controller

The detector controllers are about 15 C warmer than the ambient temperature, and the e-fold time for their temperature to change is about 10 min. In Figure 31, the power to two detector controllers had been on, and the power to the other two was turned on at t=6 min.
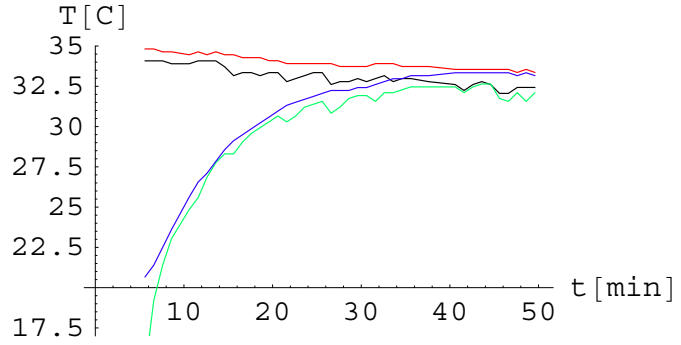
Figure 31: Temperature of the detector controllers for channel 0 (black), 1 (red), 2 (green), and 3 (blue). Power to channels 0 and 1 had been on for some time. Power had just been turned at t=6 min.

41

A   Image Parameters

We have used three parameters that indicate image quality; here we calculate them for a perfect, in-focus image. The parameter q is defined to be the amount of light in the pixels adjacent to the brightest one. Specifically,

$$q_x = (I_{-1,0} + I_{1,0})/(I_{0,0} + I_{-1,0} + I_{1,0})$$

$$q_y = (I_{0,-1} + I_{0,1})/(I_{0,0} + I_{0,-1} + I_{0,1}),$$

where $I_{0,0}$ is the intensity of the brightest pixel and $I_{i,j}$ is the intensity of the pixel offset from the brightest by (i, j). The full width is defined to be

$$w_r = 2 \left\{ \sum \left[(i - i_0)^2 + (j - j_0)^2 \right] I_{i,j} / \sum I_{i,j} \right\}^{1/2},$$

where the sum is taken over pixels whose centers are within r of the centroid (i_0, j_0). The Strehl surrogate is defined to be

$$s_r = I_{0,0} / \sum I_{i,j},$$

where the sum is taken over pixels whose centers are within r of the centroid.

λ	Res	q	w_r	s_r	r
μm			pixel		pixel
1.523	Low	0.287	1.90	0.472	2
1.523	Low	0.287	2.60	0.381	4
1.523	High	0.497	3.43	0.198	4
2.2	Low	0.465	3.48	0.216	4
2.2	High	0.587	3.22	0.122	4

Table 7: ImageParameters q, full width, and Strehl surrogate for a perfect image that is centered on a pixel. The calculation is done with the tight Lyot stops, which have a central blockage.

The values of q and the Strehl surrogate worsen as the image is moved off of the center of a pixel. The correction for q for centering (Figure 34) is

$$dq = q(x) - q(0) = \left\{ \begin{array}{c} 1.10 \\ 0.20 \\ 0.30 \\ 0.04 \end{array} \right\} x^2 \text{ for } \left\{ \begin{array}{l} 1.523\mu, \text{ low res} \\ 1.523\mu, \text{ high res} \\ 2.2\mu, \text{ low res} \\ 2.2\mu, \text{ high res} \end{array} \right\}.$$

The correction for the Strehl surrogate (Figure 32) is

$$dS = S(x) - S(0) = - \begin{Bmatrix} 0.62 \\ 0.47 \\ 0.12 \\ 0.15 \\ 0.04 \end{Bmatrix} x^2 \text{ for } \begin{Bmatrix} 1.523\mu, \text{ low res, R=2} \\ 1.523\mu, \text{ low res, R=4} \\ 1.523\mu, \text{ high res, R=4} \\ 2.2\mu, \text{ low res, R=4} \\ 2.2\mu, \text{ high res, R=4} \end{Bmatrix}.$$
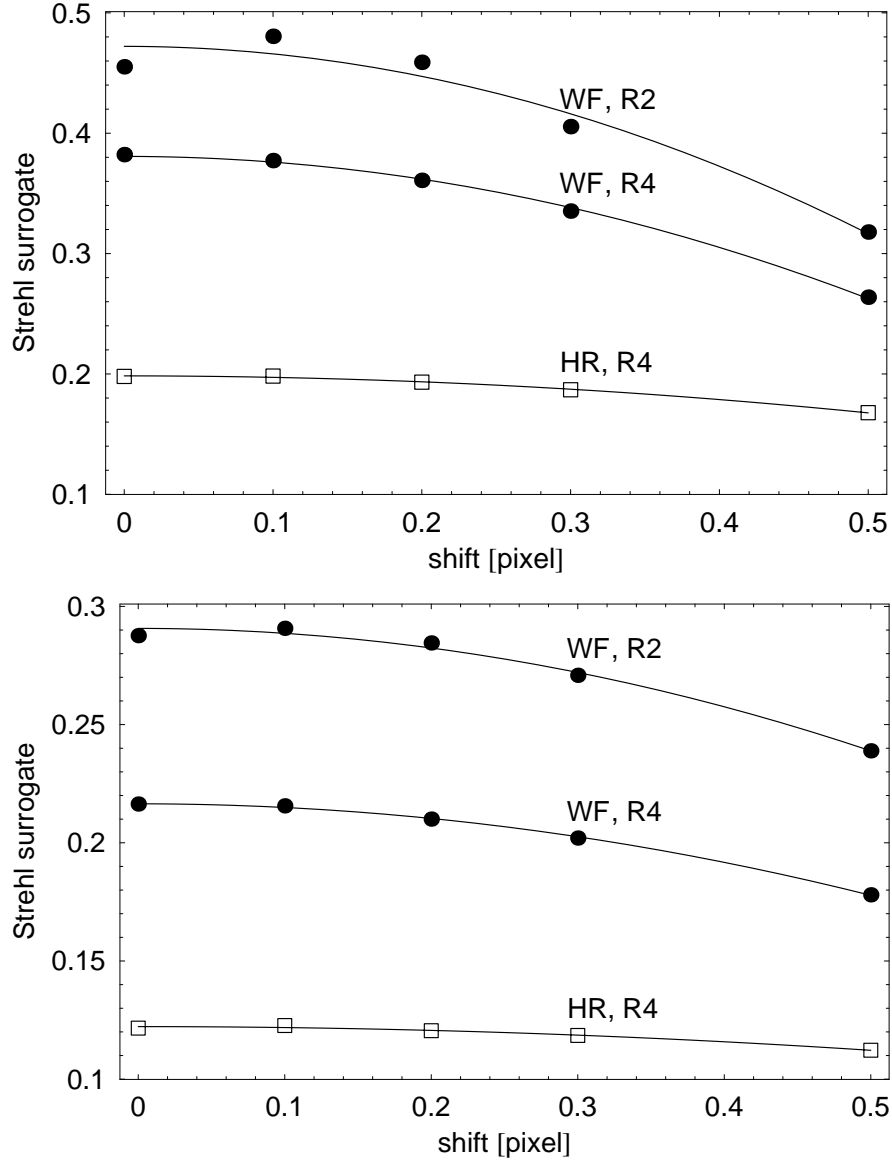
Figure 32: Strehl surrogate, the intensity in the central pixel relative to the intensity within radius R of the center, *vs.* position of the center for an ideal image at $\lambda 1.523\mu$ (top) and $\lambda 2.2\mu$ (bottom)
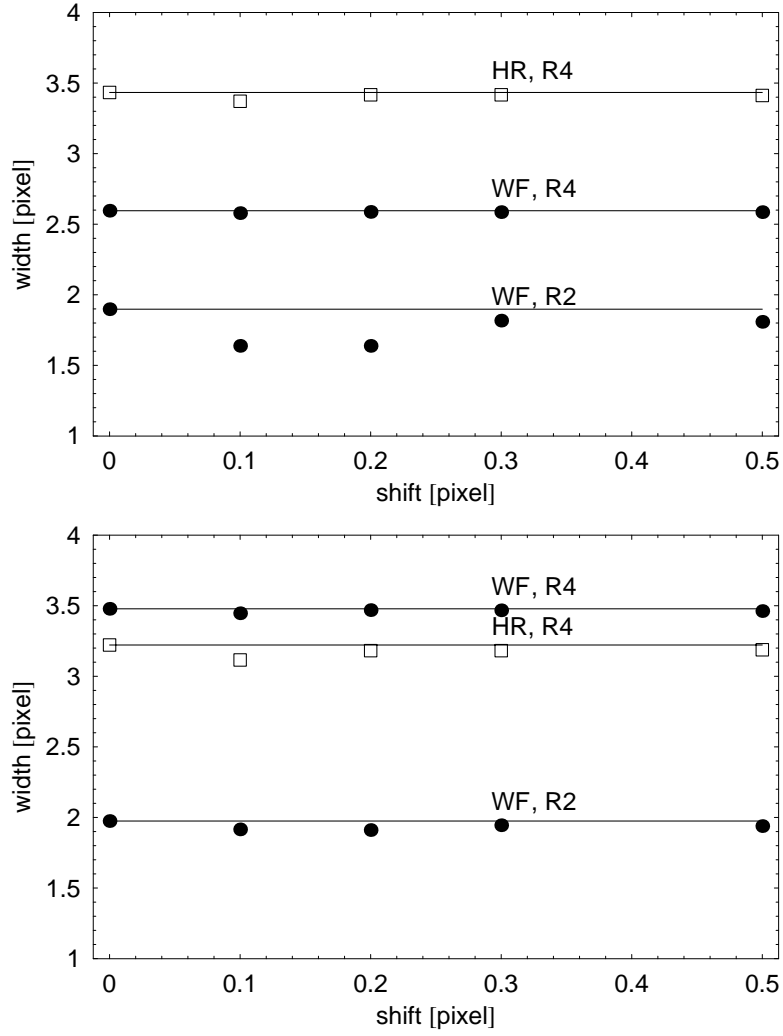
Figure 33: Image width (full, RMS) *vs.* position of the center for an ideal image at $\lambda 1.523\mu$ (top) and $\lambda 2.2\mu$ (bottom).
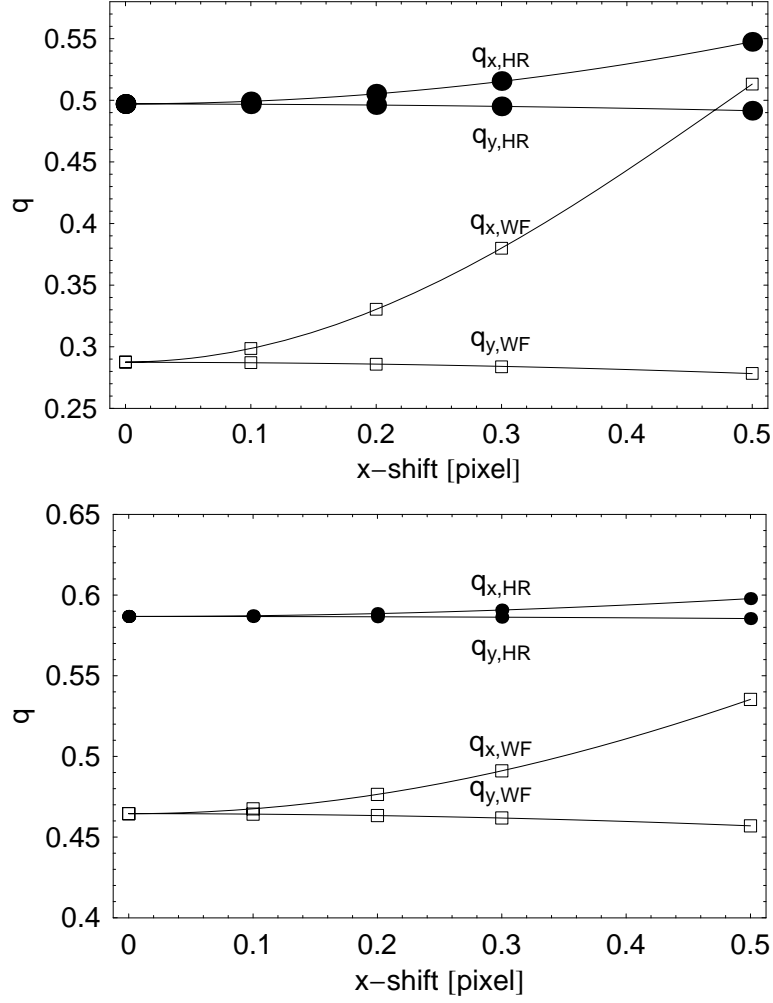
Figure 34: q_x and q_y vs x-position of the center of the image for the high-res and wide-field channels for an ideal image at $\lambda 1.523\mu$ (top) and $\lambda 2.2\mu$ (bottom).